Contents lists available at ScienceDirect

International Journal of Biological Macromolecules

journal homepage: www.elsevier.com/locate/ijbiomac

Aggregation induced nucleic acids recognition by homodimeric asymmetric monomethyne cyanine fluorochromes in mesenchymal stem cells

Nikolay Ishkitiev [a], Marina Miteva [a], Maria Micheva [b], Tanya Stoyanova [a,e], Vesela V. Lozanova [a], Valentin S. Lozanov [a], Zornitsa Mihaylova [d], Diana V. Cheshmedzhieva [e], Meglena Kandinska [e], Miroslav Rangelov [f], Nadezhda Todorova [g], Sonia Ilieva [e], Stanislav Baluschev [b,c], Raimundo Gargallo [h], Bogdan Calenic [i,**], Ileana Constantinescu [i], Katharina Landfester [b], Aleksey A. Vasilev [e,j,*]

[a] Medical University Sofia, Dept. of Medical Chemistry and Biochemistry, 2 Zdrave str., Sofia 1431, Bulgaria
[b] Max Planck Institute for Polymer Research, Ackermannweg 10, 55128 Mainz, Germany
[c] Faculty of Physics, Sofia University "St. Kliment Ohridski", 5 James Bourchier Blvd., 1164 Sofia, Bulgaria
[d] Medical University Sofia, Dept. of Oral and Maxillofacial Surgery, G. Sofijski 1 str., Sofia 1431, Bulgaria
[e] Faculty of Chemistry and Pharmacy, Sofia University "St. Kliment Ohridski", 1 James Bourchier Blvd., 1164 Sofia, Bulgaria
[f] Institute of Organic Chemistry with Center of Phytochemistry, Bulgarian Academy of Sciences, 1113 Sofia, Bulgaria
[g] Institute of Biodiversity and Ecosystem Research, Bulgarian Academy of Sciences, 1113 Sofia, Bulgaria
[h] Departament d'Enginyeria Química i Química Analítica, University of Barcelona, Martí i Franquès 1-11, E-08028 Barcelona, Spain
[i] Carol Davila University of Medicine and Pharmacy, 258 Fundeni Road, 022328 Bucharest, Romania
[j] Institute of Polymers, Bulgarian Academy of Sciences, Akad. G. Bonchev St., bl 103A, 1113 Sofia, Bulgaria

ARTICLE INFO

ABSTRACT

In the light of recent retrovirus pandemics, the issue of discovering new and diverse RNA-specific fluorochromes for research and diagnostics became of acute importance. The great majority of nucleic acid-specific probes either do not stain RNA or cannot distinguish between DNA and RNA. The versatility of polymethine dyes makes them suitable as stains for visualization, analysis, and detection of nucleic acids, proteins, and other biomolecules. We synthesized the asymmetric dicationic homodimeric monomethine cyanine dyes 1,1′-(1,3-phenylenebis(methylene))bis(4-((3-methylbenzo[d]thiazol-2(3H)-ylidene)methyl)pyridin-1-ium) bromide **(T1)** and 1,1′-(1,3-phenylenebis(methylene))bis(4-((3-methylbenzo[d]thiazol-2(3H)-ylidene)methyl)quinolin-1-ium) bromide **(M1)** and tested their binding specificity, spectral characteristics, membrane penetration in living and fixed cells, cellular toxicity, and stability of fluorescent emission. Mesenchymal cells have diverse phenotypes and extensive proliferation and differentiation properties. We found dyes **T1** and **M1** to show high photochemical stability in living mesenchymal stem cells from apical papilla (SCAP) with a strong fluorescent signal when bound to nucleic acids. We found **M1** to perform better than control fluorochrome (Hoechst 33342) for in vivo DNA visualization. **T1**, on the other hand, stains granular cellular structures resembling ribosomes in living cells and after permeabilization of the nuclear membrane stains the nucleoli and not the chromatin in the nucleus. This makes **T1** suitable for the visualization of structures rich in RNA in living and fixed cells.

1. Introduction

Fluorescence and confocal microscopy for precise observation of living cells are developing extremely rapidly [1,2]. The creation of microscopes with ever greater resolution enables a more detailed study of the structure and functions of cells and cell components [3,4]. For these reasons, there is an urgent need to develop a wide array of biomolecular probes and fluorogenic biomarkers for visualization of cells and cellular components in order to study specific processes. In this respect, it is very important to search for a greater selectivity regarding the affinity of

biomolecular labeling agents to certain biological objects. A large array of protein-target and DNA-specific probes are available [1,2,5], but selective markers for RNA-rich cell regions are very few to date [6]. Considerable efforts have been done for the development of small-molecule-based fluorescent dyes for RNA imaging in live cells [7]. Some of the structures are demonstrated below [8–12] (Scheme 1).

The weak nuclear membrane permeability of the RNA dyes is also a big disadvantage [13]. Among the most successful and promising investigations was the study of Lu and coworkers [14] who described a new RNA-selective fluorescent dye integrated with a thiazole orange and a styryl moiety (Styryl-TO) (Scheme 1). The dye shows better nucleolus-RNA staining and imaging performance in live cells than the commercial stains. The nucleolus is a dynamic subnuclear structure with roles in ribosome biogenesis, mediation of cell-stress responses and regulation of cell growth [15]. It is made by predominantly RNA, proteins and DNA and recently is mainly investigated as a target for anti RNA-virus [16,17] and anticancer therapies [18,19]. It is known that RNA viruses "hijack" the nucleolus to accelerate the production of nucleolar proteins and to facilitate the virus replication in the cytoplasm [15]. Investigating these interactions will hasten the design of new anti-viral recombinant vaccines and therapeutic molecular interventions, and also contribute to a more detailed understanding of the cell biology of the nucleolus [15–19]. The selection of an appropriate cell type is essential when testing new compounds. For a number of reasons mentioned below we picked out stem cells for the presented studies.

Stem cells are undifferentiated cells that express specific molecular markers. They can differentiate into multiple cell types and are capable of self-renewal [20]. Therefore, these cells are promising tools in the development of various methods and techniques for tissue regeneration and disease management. Two types of adult stem cells are well-known nowadays: mesenchymal stem cells (MSC) and hematopoietic stem cells (HSC) [21]. Some of the most easily accessible MSC are those of dental origin. Routinely extracted teeth are usually considered biological waste without paying attention to the properties of the non-differentiated cells they contain. The following MSC of odontogenic origin are currently known: dental pulp stem cells (DPSC), periodontal ligament stem cells (PDLSC), dental follicle stem cells (DFSC), stem cells from apical papilla (SCAP), stem cells from human exfoliated deciduous teeth (SHED) [22]. Dental MSC can differentiate into odontoblasts, cementoblasts, osteoblasts, chondroblasts, myocytes, epithelial cells, nerve cells, hepatocytes, adipocytes, etc. The specific differentiation is highly dependent on the local environmental factors, i.e., pH, growth factors, active molecules, and signals [23–25]. One of the recently studied dental stem cells are those from apical papilla (SCAP). SCAP are suitable for in vitro research with the intention of their application in regenerative medicine and bioengineering due to their rapid multiplication, easy cultivation, and ability to remain undifferentiated during division. Therefore, the design and synthesis of new fluorogenic biomolecular probes to help

visualize cellular organelles and thus the processes occurring in SCAP cells are essential to better understand and possibly manage such processes.

We believe that no other class of dyes is more suitable for visualizing biomacromolecules and cellular components than polymethine (or the so-called cyanine) dyes [5]. Their major advantage is the lack of intrinsic fluorescence in solution and the appearance of a strong fluorescent signal in the presence of the target biopolymers (DNA, RNA, proteins, etc.). The other advantages of cyanines are their convenient synthesis and easy functionalization. With the development of fluorescent spectroscopy these dyes from all subgroups are used as fluorochromes for marking and labeling cell structures and components like mitochondria [26], cell-skeletal components, DNA, RNA [27], and other bio-polymers [28] (Scheme 2).

Recently we have demonstrated that the newly prepared analogues of the commercial asymmetric monomethine cyanine dye Thiazole orange (TO) (Scheme 2a) and thiazole orange homodimer (TOTO-1) (Scheme 2b) with hydroxypropyl functionality showed strong selectivity toward GC-DNA base pairs over AT-DNA, which included both binding affinity and a strong fluorescence response. In contrast to the conventional nucleic acid stains Ethidium bromide (Scheme 2c) and its homodimer (Scheme 2d), the described by us TO and TOTO analogs demonstrate almost no intrinsic fluorescence. CD titrations showed aggregation along the polynucleotide with well-defined supramolecular chirality. The single dipyridinium-bridged dimer showed intercalation at low dye-DNA/RNA ratios. All reported in this work cyanine dyes showed potent micromolar antiproliferative activity against cancer cell lines, making them promising theragnostic agents [29]. Another recent work of our group [30] presents studies on the synthesis, improvement of the photophysical properties, and biosensing applicability of new monomethine cyanine dyes. The series of di- and tricationic dyes showed up to 5-fold enhanced resistance against photobleaching compared to the commercially available Thiazole Orange (TO) (Scheme 1a). The title compounds demonstrated their capacity as excellent fluorescent labeling agents. Depending on the dye chemical structure, current chlorine substituted Thiazole orange analogues (Cl-TO compounds) exhibit up to 834-fold enhanced fluorescence emission and form stable complexes with Calf Thymus-DNA. The calculated binding constants were found to be higher than several conventional fluorogenic dyes for nucleic acid detection. All studied derivatives appeared as less cytotoxic than the Thiazole Orange. IC_{50} concentrations in human fibroblasts MRC5 cell line were calculated up to 50 μM for the synthesized Cl-TO dyes, and 0.5 μM for the parental TO. Two of the dyes were found very competent in post-electrophoretic visualization of DNA. As demonstrated by the agarose gel electrophoresis, the staining efficiency and detection limits of the dyes were comparable to the widely used Ethidium Bromide (Scheme 2c) but without the typical for this dye intrinsic fluorescence. The tricationic dye revealed great potential for cell cycle analysis in G1, S, and G2 phases. We proved that the chlorinated TO derivatives readily stain human cells in vivo, while they can effectively be applied for eukaryotic and microbial cell staining [30]. In another study, we demonstrate the successful nucleic acids staining ability of a series of asymmetric monomeric monomethine cyanine dyes with chlorine and trifluoromethyl functionality [31]. The dyes show ratiometric red shift of their longer wavelength absorption maxima. It is in the range 514–522 nm neat in TE buffer, 516–528 nm in the presence of DNA, and 518–524 nm in the presence of RNA. Practically the target dyes are not fluorescent in water solutions or possess negligible fluorescence, but become strongly fluorescent after contacting with nucleic acids. Molecular docking studies have been performed to investigate the nature of binding mode of the dyes with DNA. The dicationic chlorine containing analogues are groove binders and the trifluoromethyl substituted dyes with the bulky substituents are interacting with DNA through partial intercalation mode. A considerable increase of the fluorescence intensity upon binding to RNA compared to dsDNA is observed particularly in the group of chlorine substituted groove binders
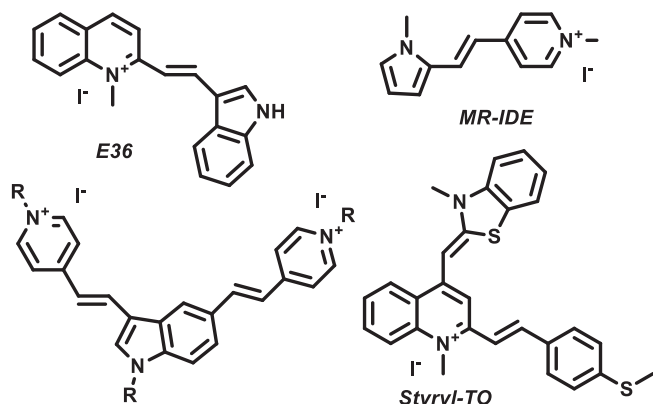
Scheme 1. Chemical structures of most promising RNA selective dyes.

E36

MR-IDE

Styryl-TO
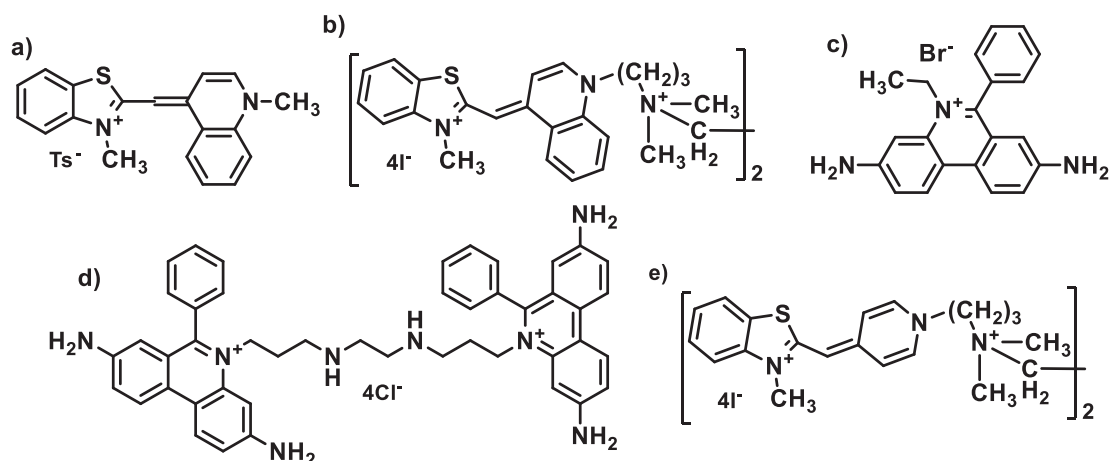
Scheme 2. Chemical structures of the most prominent dyes for bioanalysis: a) Thiazole orange (TO) b) Thiazole orange homodimer – TOTO-1; c) Ethidium bromide; d) Ethidium homodimer; e) BOBO-1.

[31]. The discussed above useful properties of the Thiazole orange analogues demonstrate that the fine tuning of their chemical structure leads to improving their properties in the desired way and ensures higher selectivity of binding the dyes to definite biomolecules. All these valuable results were the stimulus to design new representatives of these interesting class of dyes and to check their potential application as fluorogenic cell stains.

A main problem in the biomolecular recognition of nucleic acids is that the chemical composition of DNA and RNA is quite similar and for real identification of nucleic acids is important to design very sensitive dyes. These probes must recognize small differences in molecular structure, which in turn cause significant changes in their photophysical properties and the commented phenomena should be observed in living cells as well. A more accessible implementation is the use of the aggregation phenomenon called aggregachromism. In different forms of aggregation, dyes of the cyanine class are known to exhibit a number of interesting photophysical manifestations [32]. Our idea is to use the corresponding nucleic acid as a kind of biological matrix on which, based on specific spatial interactions, aggregachrome aggregates can be bind or even built. The challenges presented so far made us ambitious to look for suitable molecular structures that, based on dynamic aggregation states, would provide the desired selectivity. To accomplish this goal, we used a Thiazole Orange backbone linked by a short and hindered spacer. The chemical structures of the target dyes are selected to accelerate the formation of different semi-stable aggregates in free state and in presence of nucleic acids with subsequent change in the photophysical properties of dye-NA complex. Due to the huge interest in the properties and application of stem cells we used them as an object of our combined studies.

The present work aims to check the role of two newly developed homodimeric asymmetric polycationic monomethyne cyanine dyes (analogues to TOTO-1 and BOBO-1, Scheme 2b and e) as cell components binding fluorogenic markers in dental mesenchymal stem cells, to study dye penetration, fluorescence intensity, cellular toxicity, and effects on cell cycle and proliferation of SCAP. The specific design of the presented structures (Scheme 2a-e) is justified in order to create prerequisites for a different arrangement of molecules and the formation of different aggregates depending on the surrounding environment or after interaction with a certain biomatrix. The purpose of this aggregation diversity is to observe a different absorption and fluorescence response, because of the contact with the target bio-objects.

2. Experimental

2.1. General

All solvents used in the present work are HPLC grade and commercially available. The starting materials **1a**, **1b**, and **1c** are commercially available and they were used as supplied. Melting points of **T1** and **M1** were determined on a Büchi MP B-545 apparatus and are uncorrected. *NMR spectra* (^{1}H-, ^{13}C NMR) were obtained on a Bruker Avance II + NMR spectrometer operating at 500 MHz for ^{1}H- and 125 MHz for ^{13}C NMR in DMSO-d_6 as a solvent. The chemical shifts are given in ppm (δ) using tetramethylsilane (TMS) as an internal standard. UV-VIS spectra were measured on Evolution 350 (Thermo Scientific) UV–VIS spectrophotometer and the fluorescence spectra were obtained on a Cary Eclipse (Agilent) fluorescence spectrophotometer in the Institute of Polymers, Bulgarian Academy of Sciences. The fluorescence spectra of dyes **T1** and **M1** with RNA in formalin and in presence of BSA respectively were measured on ***Fluorolog 3*** in Sofia University. Fresh stock solutions (1 mM) were prepared in DMSO, and further diluted with TE-buffer (Tris-HCl 10 mM pH 8.0; EDTA 1 mM, pH 8.0) to 1.10^{-5} M for the UV–VIS spectra and to 1.10^{-6} M for the fluorescence spectra. The salmon sperm dsDNA (CAS 68938–01-2) and baker's yeast RNA (CAS 63231–63-0) were purchased from Merck (Sigma-Aldrich) and used as received. The stock concentrations of DNA and RNA were 1 mg/mL stock. The purity of the nucleic acids was checked by the absorption spectrum and the ratio at 260–280 nm. The operating concentration of the DNA and RNA working solutions was defined spectroscopically following molar extinction coefficients at the wavelengths indicated: dsDNA – 6600 M^{-1}, RNA - 7800 L.mol^{-1}.cm^{-1} [33a]. The intermediates **2a-c** were synthesized by a method described in the literature [29–31]. The *MALDI-TOF/TOF* spectra were measured on a Bruker rapifleX platform at the MPIP, Mainz, Germany. *Liquid chromatography mass spectrometry analysis (LC-MS).* The analyses were carried out on Q Exactive® hybrid quadrupole-Orbitrap® mass spectrometer (Thermo-Scientific Co, USA) equipped with a HESI® (heated electrospray ionization) module, TurboFlow® Ultra High Performance Liquid Chromatography (UHPLC) system (ThermoScientific Co, USA) and HTC PAL® autosampler (CTC Analytics, Switzerland). Chromatographic conditions: The chromatographic separations of the analyzed compounds was achieved on Nucleodur C18 Isis (150 × 2.1 mm, 3.5 μm) analytical column (Macherey-Nagel, Germany). using gradient elution at 300 L/min flow rate. The used eluents were: A - 0.1 % formic acid in water; B - 0.1 % formic acid in ACN. Mass spectrometry conditions: Full-scan mass spectra over the *m/z* range 100–1500 were acquired in positive ion mode at resolution settings of 70,000. The mass spectrometer

operating parameters used in a positive ionization mode were: spray voltage - 4.0 kV; capillary temperature - 320 °C; probe heater temperature - 300 °C; sheath gas flow rate 27 units; auxiliary gas flow 7 units; sweep gas 2 units (units refer to arbitrary values set by the Q Exactive Tune software) and S-Lens RF level of 50. Nitrogen was used for sample nebulization and collision gas in the HCD cell. The main ions are [M + 2H]$^+$. Data acquisition and processing were carried out with XCalibur® ver 2.4 software package (ThermoScientific Co, USA). *Circular dichroism (CD).* CD measurements were conducted at 25 °C using a JASCO J1500 Circular Dichroism Spectrophotometer in Max Planck Institute for Polymer Research, Mainz, Germany. The following experimental parameters were used: path length of the cell (10 mm), scan rate (50 nm/min), scan range (600–200 nm), data pitch (1.0 nm), and data integration time (8 s). Solutions of dyes **T1** and **M1** with initial concentration 10 mM in DMSO were added to the respective DNA or RNA solution as follows: DNA solution 3.0 mg/mL and RNA 2.4 mg/mL in TE buffer (Tris-HCl 10 mM, EDTA 1 mM) at pH 7.4. Stem cells from apical papilla (SCAP) were isolated from non-fully developed third molars ($n = 10$), Deciduous teeth and mucosa were supplied by patients undergoing routine deciduous tooth extraction at Dental Faculty Hospital, Medical University, Sofia, Bulgaria. The study was conducted in accordance with the Declaration of Helsinki. All patients participating in the study signed an informed consent form following the decision of the Ethical Committee of Medical University, Sofia's Council of Medical Science (No. 4770\11.12.2018) after signing informed consent by the patients. The apical papilla was gently removed from the apex of the developing root and stored for digestion in a solution of 3 mg/mL collagenase type I and 4 mg/mL dispase (Sigma-Aldrich, St. Louis, MO, USA) for 1 h at 37 °C in the incubator. The cells were grown with Dulbecco's modified Eagle's medium (DMEM) (Invitrogen, Eugene, OR, USA) supplemented with 1 % antibiotic-antimycotic (Invitrogen) and 10 % heat-inactivated fetal bovine serum (FBS) (Sigma-Aldrich). Cells between 3 and 5 passages were used for the experiments. *Fluorescence imaging of cells.* Fluorescence of non-fixed and formalin-fixed SCAP was performed. Non-fixed SCAP were seeded in 96-well plates (TPP Techno Plastic Products AG, Trasadingen, Switzerland) at a density of 1×10^5 cells/cm^2. Cells were then incubated for 48 h to 72 h at standard cell culture conditions until reaching sub-confluence. The medium was changed with Phenol red-free DMEM in order to avoid visualization results alterations by reducing lateral scattering and uptake by phenol red in the medium. Dyes **T1** and **M1** at concentrations of 1 mM, 0.1 mM, and 0.01 mM were added to the wells. Hoechst 33342 dye was used as a positive control, as it stains the nuclei of living cells at concentrations of 0.01 mM. The 96-well plate was incubated for 24 h in the dark under standard conditions (37 °C and 5 % CO$_2$) until dyes penetrate the cells. The staining was detected after 24 h, 48 h, and 72 h. The analysis was performed on a confocal fluorescence microscope In Cell Analyzer 6000 (GE Healthcare, Chicago, Illinois, United States). Formalin-fixed SCAP were incubated with 1 mM and 10 mM **T1** and **M1** dyes. Cells stained with 4′,6-diamidino-2-phenylindole (DAPI), were used as control. The effect of the **T1** and **M1** dyes on cellular proliferation was assessed via MTT Cell Proliferation Assay Kit (Novus Bio, Littletown, CO, USA) following the manufacturer's instructions. SCAP were seeded on a 96-well plate with phenol red free DMEM supplemented with 10 % FBS. M1 and T1 dyes were added at a final concentration of 1 mM and incubated for 24 h at standard cell culture conditions. The analysis of the data was performed via microplate reader (Varioscan, Thermo Scientific) at 590 nm wavelength. *Density functional theory (DFT) quantum chemical computations.* Density functional theory (DFT) quantum chemical computations at B3LYP /6-31G(d,p) level were applied for geometry optimization of the dye ligands and their complexes with DNA. Docking studies were performed to examine the favorite ways of interaction of the cyanine dyes with double-strand DNA (dsDNA) and double-strand RNA (dsRNA). Several potential ways of interaction were explored: minor or major groove binding and intercalation into the NA helix. A series of 3D XRD structures were sorted out and employed as docking templates. The selected PDB codes of dsDNA structures were as follows: 108D, 185D, 1DNE, 1XRW, 1Z3F, 2DES. Excluding only 1DNE, other complexes represent dsDNA with an intercalated ligand. 1DNE was used as a kind of control for the possible formation of complex alongside DNA grooves. To probe this opportunity the ligand from 1DNE was removed and the method of Edelsbrunner [34] was used to specify centers along the minor and major grooves, as it is implemented in the MOE software [35]. Defined in such a way, they were further applied for positioning ligands in the grooves for the docking procedure. In other XRD structures the position of the ligand in the crystallized complex was used to direct the placement of our ligands. The process of intercalation results in a cavity in dsDNA, with the best possible size for the intercalating molecule, therefore we have chosen the Induced Fit methodology for the docking of our ligands. To relax XRD structures and to condition them in a solution we performed short (50 ns) molecular dynamics (MD) simulations with NAMD software. AMBER12EHT force field and explicit water molecules in periodic boundary conditions at 310 K for all XRD structures were applied. The dsRNA models were set up based on the modification of the same dsDNA XRD structures to dsRNA constructs, followed by 250 ns molecular dynamics simulation with the same simulation parameters as for dsDNA. The following possibilities arise for interaction between the ligands and nucleic acids: in the major groove; in the minor groove; single (mono) intercalator; bis intercalator - 1,2,3, and 4 base pairs away.

2.2. Synthesis of 1,1′-(1,3-phenylenebis(methylene))bis(4-methylpyridin-1-ium) bromide (2a) and 1,1′-(1,3-phenylenebis(methylene))bis(4-methylquinolin-1-ium) bromide (2b)

In a 100 mL round-bottom flask equipped with an electromagnetic stirrer and reflux condenser were added 3 g (0.0114 mol) of 1,3-bis(bromomethyl) benzene and 2.3 fold molar excess of γ-picoline or 2.3 fold molar excess of lepidine. The mixture was dissolved in 20 mL *N*-Methyl-2-pyrrolidone (NMP) and heated at 120 °C under vigorous stirring for six hours. After cooling to room temperature, 50 mL of acetone was added and the resulting white precipitate was filtered through a Buchner funnel, washed with three 30 mL portions of acetone and dried in a desiccator. The resulting new quaternary compounds **2a** and **2b** are novel, not previously described in the literature. They are highly hygroscopic, which makes it difficult to characterize them. Their chemical structure is proven by the structure of the target dyes. Yield **2a**: 71 %, **2b**: 54 %.

2.3. Synthesis of 1,1′-(1,3-phenylenebis(methylene))bis(4-((3-methylbenzo[d]thiazol-2(3H)-ylidene)methyl)pyridin-1-ium) bromide (T1) and 1,1′-(1,3-phenylenebis(methylene))bis(4-((3-methylbenzo[d]thiazol-2(3H)-ylidene)methyl)quinolin-1-ium) bromide (M1)

2.43 g (0.0054 mol) 1,1′-(1,3-phenylenebis(methylene))bis(4-methylpyridin-1-ium) bromide (**2a**) or 3 g (0.0054 mol) 1,1′-(1,3-phenylenebis(methylene))bis(4-methylquinolin-1-ium) bromide (**2b**) and 3.52 g (0.011 mol) 2-methylmercapto-3-methylbenzo[*d*]thiazolium methyl sulfate are mixed and ground into a mortar. The well-ground mixture was quantitatively transferred to a 50 mL round-bottom flask and 10 mL acetic anhydride is added to the mixture. The reaction flask is fitted with a reflux condenser connected to a vessel with 1M aqueous solution of potassium hydroxide through which methyl mercaptan evolved during the reaction bubbled. The mercaptan is captured by chemisorption in the potassium hydroxide solution. The mixture was stirred vigorously without heating for more than 3 h. 30 mL of diethyl ether and 10 mL acetone were added thereto and the resulting precipitate was filtered off and dried. Yield of crude products:

T1 = 2.44 г (61 %) and **M1** = 3.70 g (80 %). An analytical sample of the dye described is obtained after fractional recrystallization from methanol. **T1**: Tt = 261-262 °C. ^{1}H NMR (500 MHz, DMSO-d_6, TMS, δ (ppm)): 3.68 s (6H, CH$_3$), 5.49 s (4H, CH$_2$), 6.27 s (2H, CH), 7.24 s (1H,

CH), 7.27–7.34 m (2H, CH), 7.38 d (4H, $^3J_{HH}$ = 7.2 Hz, CH), 7.43 brs (1H, CH), 7.46 brs (2H, CH), 7.50–7.56 m (5H, CH), 7.89 d (2H, $^3J_{HH}$ = 7.9 Hz, CH), 8.38 d (4H, $^3J_{HH}$ = 7.2 Hz, CH); ^{13}C NMR (δ (ppm), DMSO-d_6, DEPT 135 (125 MHz)): 32.85 (CH3), 52.76 (CH), 59.74(CH$_2$), 89.86 (CH), 112.18 (CH), 122.49 (CH), 123.67 (CH), 126.67 (CH), 127.85 (CH), 128.16 (CH), 129.79 (CH), 132.13 (CH), 131.13 (CH), 141.36 (CH). MALDI-TOF (m/z) Calculated Chemical Formula: $C_{22}H_{21}N_2S^+$, Calc. Exact Mass: 344,13 Found [M/2z]$^+$: 344.1635, Found (m/z): 695.2374. HPLC-ESI-MS: Calculated Chemical Formula: $C_{18}H_{16}N_2S^{3\bullet+}$ Exact Mass: 292.10, Found: Found [M + 3H]$^{3+}$: 292.12976.

M1: T_T = 257-258°C. ^{1}H NMR (500 MHz, DMSO-d_6, TMS, δ (ppm)): 3.93 s (6H, NCH$_3$), 5.80 s (4H, N$^+$CH$_2$), 6.10 s (1H, CH, Ar), 6.83 s (2H, -CH=), 7.17 d (2H, J$^3_{HH}$ = 7.2 Hz, CH, Ar), 7.29 dd (2H, J$^3_{HH}$ = 7.5 Hz, CH, Ar), 7.42 d (2H, J$^3_{HH}$ = 7.7 Hz, CH, Ar), 7.49–7.61 m (11H, CH, Ar), 7.87 d (2H, J$^3_{HH}$ = 7.8 Hz, CH, Ar), 8.53 d (2H, J$^3_{HH}$ = 7.2 Hz, CH, Ar), 8.65 dd (2H, J$^3_{HH}$ = 5.4 Hz, J$^3_{HH}$ = 9.7 Hz, CH, Ar). ^{13}C NMR (δ (ppm), DMSO-d_6, DEPT 135 (125 MHz)): 34.32 (CH$_3$), 53.27 (CH), 56.75 (CH$_2$), 89.23 (CH), 107.61 (CH), 107.68 (CH), 113.50 (CH), 118.53 (CH), 121.81 (CH), 123.11 (CH), 125.05 (CH), 126.25 (CH), 126.62 (CH), 127.17 (CH), 128.66 (CH), 130.19 (CH), 133.24 (CH), 144.94 (CH). MALDI-TOF (m/z) Calculated Chemical Formula: $C_{26}H_{23}N_2S^+$, Exact Mass: 394,54 Found [M/2z]$^+$: 394.1487; HPLC-ESI-MS: Calculated Chemical Formula: $C_{22}H_{18}N_2S^{3\bullet+}$ Exact Mass: 342.12, Found: Found [M + 3H]$^{3+}$: 342.13940.

3. Results and discussion

3.1. Synthesis

Several common methods for the preparation of monomethine cyanine dyes are known so far [5,33]. The first monomethine cyanine dyes were prepared [36] by heating an alcoholic or aqueous solution containing a salt of quinoline and one of lepidine or quinaldine with caustic alkali, whereby reaction proceeded according to Scheme 3a.

Another frequently used method for the synthesis of symmetrical and nonsymmetrical monomethine cyanine dyes is the synthesis developed by Brooker et al. (Scheme 3b) [37]. It is based on the reaction between 2-methylthiobenzothiazolium and quaternized quinolinium salts (Scheme 3b). By this method were prepared most of the commercial products of the US biochemical company Molecular Probes, Inc. nowadays part of Thermo Fisher Scientific [38] like TO, TOTO-1, BOBO-1, PO-PRO-1, BO-PRO-1, YO-PRO-1, and TO-PRO-1 as well as the most used for PCR assay dyes SYBR Safe, SYBR Green I, Pico Green and others [38].

A new method for the preparation of symmetric and asymmetric monomethine cyanine dyes on the solvent-free condensation of various active methyl group-containing quaternized heterocycles with zwitter-ionic quinolinium compounds is reported (Scheme 3c) [39]. The condensation is carried out in the absence of a basic reagent which gives the opportunity to use some unstable in basic conditions heterocycles.

A synthetic method described firstly by Brooker was modified by Deligeorgiev and coworkers [40] and used for preparation of poly-cationic analogs of TO (Scheme 3d). Vasilev et al. proposed alternative way avoiding the Hoffmann elimination side reactions typical for the former procedure and the photo induced bis-condensation of chlor-oquinolines [41] (Scheme 3d).

Among the listed above synthetic methods the Brookr's method remains the most commonly used when methyl substituents are linked to the benzothiazolium heterocycle (unwanted exchange of the different S-alkyl and N-alkyl substituents connected to the benzothiazole ring were detected [37]) despite the shortcomings like the release of mercaptans. Due to the specificity of the target product, we chose to carry out the reaction for the production of dyes **T1** and **M1** by this method. For this purpose, it was necessary to synthesize the intermediates 1,1′-(1,3-phenylenebis(methylene))-bis-(4-methylpiridinium-1-yl) bromide (**2a**) and 1,1′-(1,3-phenylenebis(methylene))-bis-(4-methylquinolin-1-yl) bromide (**2b**) by quaternization reaction of 1,1′-(1,3-phenylenebis (methylene))bis(4-methylquinolin-1-yl) bromide (**1a**) (Scheme 4).

The quaternization reaction was performed in the high boiling and highly polar solvent *N*-Methyl-2-pyrrolidone (NMP). Our attempts to avoid the solvents and to perform the synthesis in a green manner failed due to the low solubility of the mono quaternized product. Therefore, we had to search for a suitable high boiling solvent. The non-polar solvents like toluene or nitrobenzene afforded very long reaction times and low yields. Finally, NMP appeared the most suitable for this synthesis ensuring shorter reaction times and higher yields. The molar ratio between *m*-dibromomethylbenzene (**1a**) and respectively the γ-picoline (**1b**) or the lepidine (**1c**) is more than double molar excess of the *N*-containing base **1b** or **1c**. The progress of the reaction was monitored by thin layer chromatography (eluent dichloromethane / methanol = 10: 2). The resulting quaternary product is highly hygroscopic therefore its structure has been proven by elucidating the chemical structure of the target dyes **T1, M1**. The condensation reaction between the dicationic quaternary salts (**2a** and **2b**) and 1-methyl-2-methylmercapto benzo-thiazole methyl sulfate (**2c**) in the presence of *N*-ethyl-diisopropylamine (DIPEA) as the basic reagent afforded the target dyes **T1** and **M1** with very good to excellent yields (Scheme 4 and Scheme 5).

The emission of methyl mercaptan released during the reaction was captured by bubbling the outgoing gas through a reaction vessel with saturated aqueous solution of potassium hydroxide. The dyes were purified by fractional recrystallization from methanol. Its chemical structures and purity were proved by NMR, HPLC-MS, UV-VIS and fluorescence spectroscopy and are presented in Scheme 4 and Scheme 5, in the experimental part and in the SI. As already mentioned, the design of the obtained new homodimeric dyes is focused on the specific orientation on the surface of the bio-objects and their behavior in living cells. In this way, we aim to obtain biomarkers suitable for biomolecular
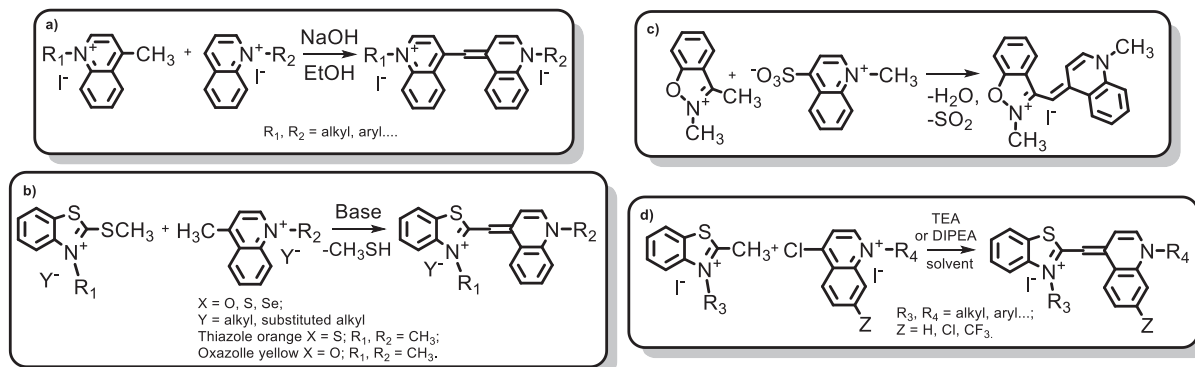
Scheme 3. a) The first method for synthesis of monomethine cyanine dyes; **b)** The Brooker's method. **c)** Knoevenagel-type condensation of methyl-benzoisoxazole and 4-sulfoquinolinium salts; **d)** Condensation between 2-methylbenzothiazolium salts and 4-chloroquinolinium quaternary compounds.
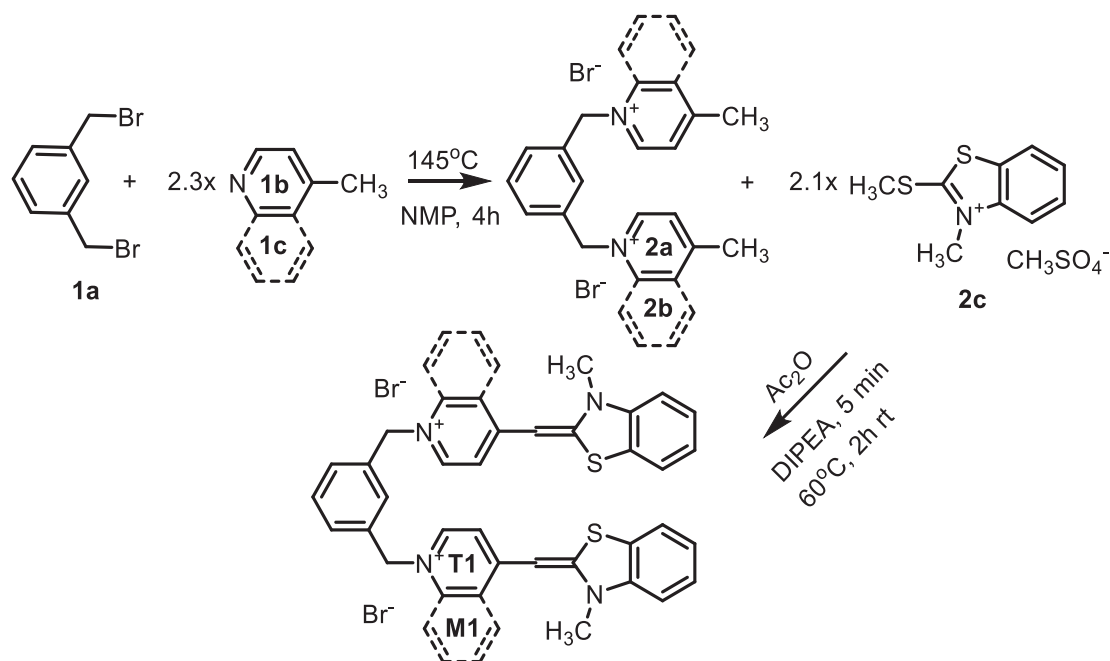
Scheme 4. Synthetic pathway for preparation of dyes **T1** and **M1**.
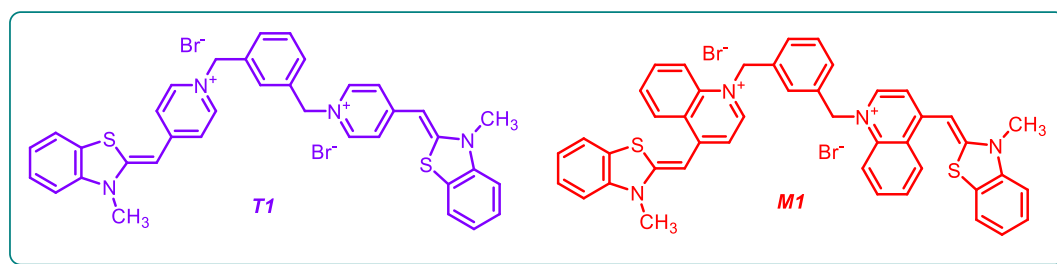
Scheme 5. Chemical structures of the homodimeric asymmetric monomethine cyanine dyes **T1** and **M1**.

recognition based on aggregation phenomena.

3.2. Photophysical properties of T1 and M1

3.2.1. Absorption

The absorption spectra of the dyes were measured in TE buffer. Dye **T1** demonstrates an absorption band and a bathochromic shoulder. The blue shifted absorption band in the visible spectrum is at 428 nm with very high molar absorptivity at $140400 L.mol^{-1}.cm^{-1}$ (Fig. S1a) corresponding probably to an intramolecular H-aggregate (plane-to-plane stacking) [32]. The dilution of the solution, warming to 50 °C and sonication for at least 15 min do not change the form and the position of the maximum. The second pick is at 455 nm with moderate molar absorptivity of $30,920 L.mol^{-1}.cm^{-1}$ and can be assigned to the monomolecular form of the dye. Dye **M1** is characterized by one absorption maximum and two shoulders (Fig. S1b). The shorter wavelength maximum is at 452 nm with molar absorptivity $59,000 L.mol^{-1}.cm^{-1}$. The most intensive pick in the visible spectra is at 475 nm with molar absorptivity $129,440 L.mol^{-1}.cm^{-1}$ denoted to the monomer [32]. The third signal is a bathochromic shoulder at 505 nm with molar absorptivity $32,540 L.mol^{-1}.cm^{-1}$. Fig. 1a presents the change in visible light absorption of dye **T1** by increasing the amount of double-stranded DNA (dsDNA). Dye **T1** could be denoted as structure analogue of the homodimeric monomethine cyanine dye BOBO-1 (Scheme 2e). According literature data the longest absorption maxima of BOBO-1 is at 462 nm in water [42] correlating to the maximum at 455 nm in the spectrum of our

dye **T1** (Fig. 1a). Successive addition of DNA to dye **T1** buffer solution results in a proportional decrease of the most intense band in the visible spectrum at 430 nm (Fig. 1a). Conversely, with increasing double-stranded DNA concentration, a slight increase in the intensity of the bathochromic band at 455 nm was observed (Fig. 1a). Generally, the observed bathochromic shift combined with decrease of the longest absorption maximum of the visible spectra of monomethine cyanine dyes points out to the intercalation of the dyes into nucleic acids due to the interaction between the π-electrons of the chromophore and those of the corresponding nucleobases [26,27]. Surprisingly the absorption band of **T1** typical for the absorption of monomeric form at 455 nm only slightly increases (Fig. 1a and b). Similar is the situation with the absorption spectra of **T1** in presence of RNA (Fig. 1c, d). The decrease of the absorption at 430 nm most probably could be explained by the decomposition of quays stabile intramolecular H-aggregates followed by their nucleic acid interaction. According to Kumar et al. [43] the groove binding mode can be characterized with slight bathochromic shift and hyperchromic shift of the longest absorption maximum of the dyes after nucleic acid binding, which actually happened with the 455 nm and 457 nm maxima after T1-DNA and T1-RNA complexes formation (seen respectively in Fig. 1a and b).

The discussed above phenomena indicate for possible groove binding mode of **T1** to the nucleic acids or groove binding combined with partial intercalation. The absorption behavior registered with dye **M1** (Fig. 1c and d) is a bit different. The absorption at 475 nm typical for the H-aggregate for TO dyes decreases increasing the concentration of
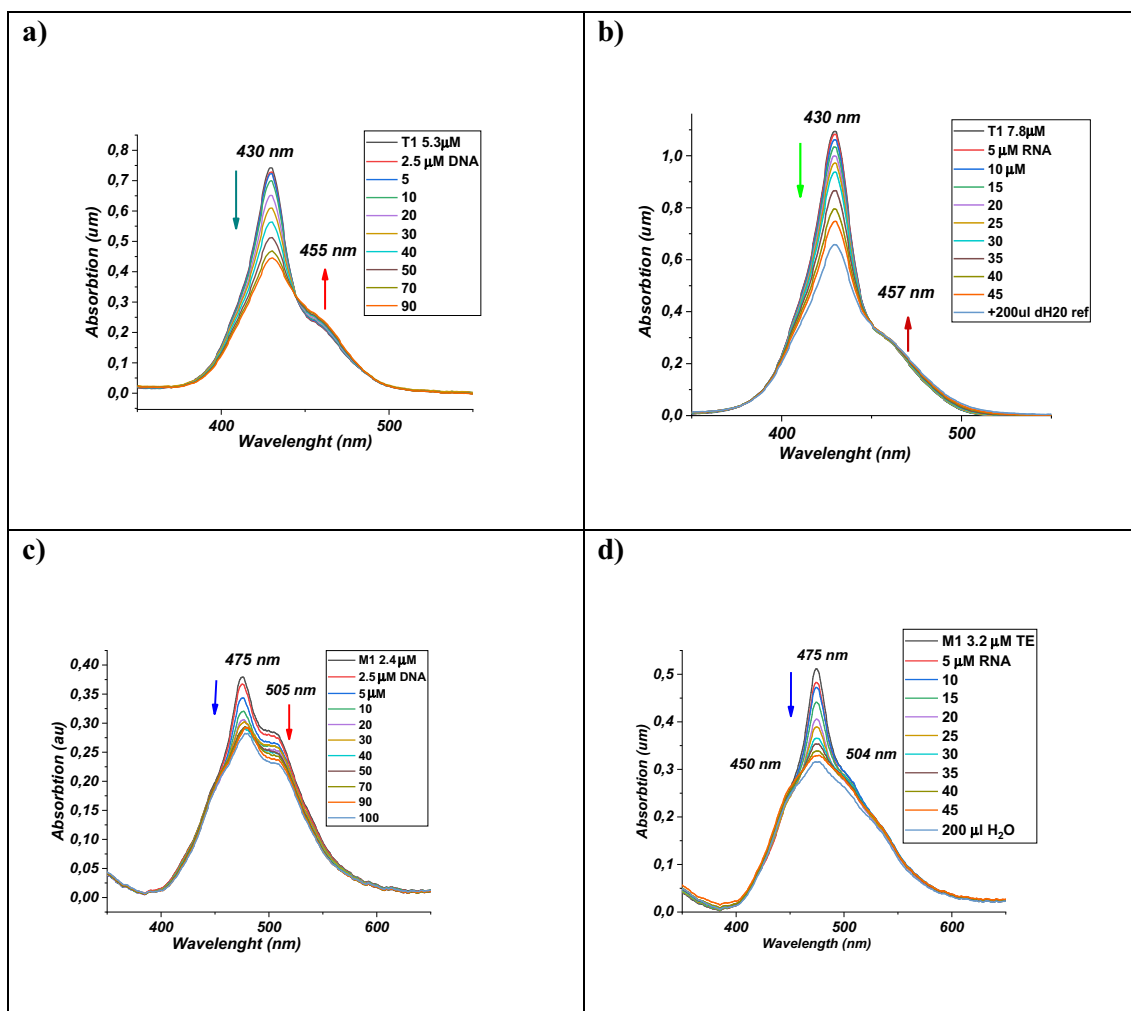
Fig. 1. a). Absorption intensity dependence of dye **T1** as a function of dsDNA concentration; **b)** Absorption intensity of dye **T1** as a function of RNA concentration; **c)** Absorption intensity dependence of dye **M1** as a function of dsDNA concentration with 2.5 μM of dsDNA step; **d)** Absorption intensity dependence of dye **M1** as a function of RNA concentration with 5 μM of RNA step.

appropriate nucleic acid due to nucleic acid induced aggregate disruption. Consequently, a hypochromic shift of the absorption at 475 nm is observed. The absorption maximum at 505 nm corresponding to the monomer form of the dye decreases increasing the amount of nucleic acid [42] suggesting an intercalation mode of binding (Fig. 1c and d) [43]. In order to prove the correctness of the conclusions made about the type of binding between dyes **T1** and **M1**, and the target nucleic acids, we used one of the most informative and accessible methods – Circular dichroism.

3.2.2. Circular dichroism study of the interaction of dyes T1 and M1 with dsDNA and yeast RNA

Circular dichroism (CD) spectroscopy was used to assess the interaction of both dyes with the considered nucleic acids. CD may be used to gain insight into the binding mode of dyes to duplex DNA [42]. In principle, non-chiral molecules exhibit no CD signal in solution. However, when a non-chiral ligand binds to a chiral host, such as DNA, a new induced CD (ICD) signal appears in the wavelength region corresponding to the absorbance of the bound compound. Intercalating dyes usually produce negative or very small positive ICD signals. Groove binding is generally indicated by the presence of a large positive ICD signal. Cyanine derivatives, which may form stacked complexes in the minor groove of duplex DNAs, exhibit strong exciton splitting [44,45]. Fig. S2 shows the CD spectra recorded along the titration of dsDNA

with **T1**. The CD spectrum of dsDNA shows positive and negative bands at 280 and 240 nm, respectively, being the intensity of the positive band approximately twice that of the negative band. These features denote a B-DNA conformation. As expected, any signal is observed in the visible region. Upon addition of the **T1** dye, the intensity of the bands in the UV region decreases, whereas ICD signals appear in the visible region of the spectra. A similar trend was observed along the other titrations (Fig. S2b-d). In some cases, the observed changes in intensity and position of the ICD along the titration pointed out to the existence of intermediate species. To have a more detailed description of the steps in which the interaction process occurs, the CD spectra recorded along the titrations were analyzed with a multivariate data analysis method, the Multivariate Curve Resolution based on Alternating Least Squares [46]. This method analyzes the whole CD data set allowing the determination of the number of components (usually, chemical species) present along the experiment, as well as the calculation of the corresponding distribution profiles and their pure spectra. Fig. 2 shows the results obtained after the analysis of the CD spectra of each titration with the MCR-ALS method.

The interaction of **T1** with dsDNA along the titration may be explained with two species. The first one, depicted in blue, corresponds to the dsDNA. The second one, depicted in red, corresponds to the species formed from the interaction of **T1** with dsDNA. The pure spectrum of this species reveals the reduction of the intensity of CD bands in
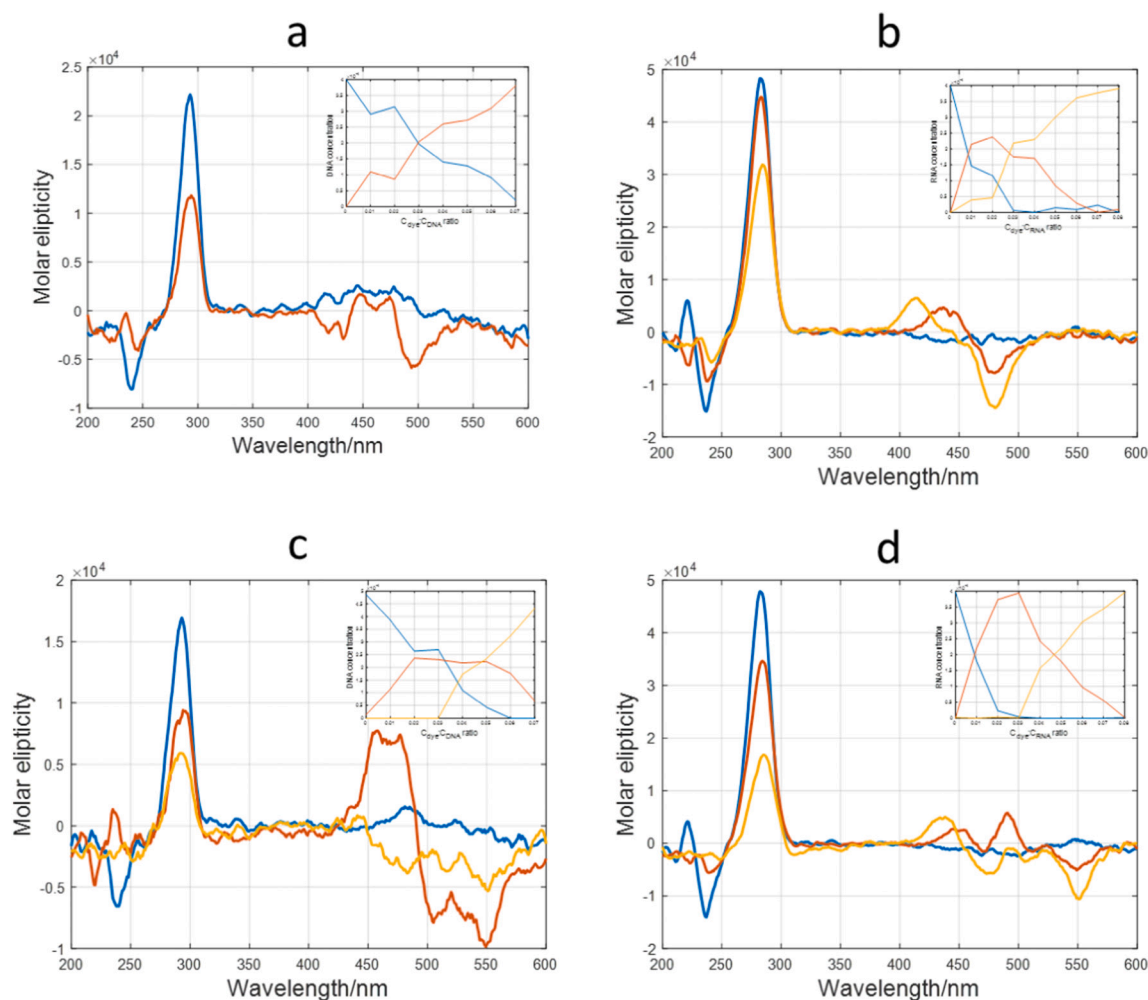
Fig. 2. Distribution profiles and pure spectra obtained with MCR-ALS from the analysis of the CD spectra recorded for each one of the titrations. (**a**) dsDNA with **T1**, (**b**) RNA with **T1**, (**c**) dsDNA with **M1**, (**d**) RNA with **M1**. Insets show the corresponding distribution profiles. In all cases, blue denotes the initial dsDNA or RNA species. Species depicted in red and yellow are related to the successive modes of interaction observed along the titration. (For interpretation of the references to colour in this figure legend, the reader is referred to the web version of this article.)

the UV region, which could be related to distortion of the initial B-DNA upon binding of the dye. The pure spectrum of this species also shows a weak negative ICD signal, which could be explained as an effect of the intercalation [43].

A slightly different situation is observed along the titration of RNA with **T1**. In this case, the CD spectra recorded along the titration were explained satisfactorily with three species (Fig. 1b). Again, the blue one corresponds to the initial nucleic acid (here, RNA). The red and yellow species would correspond to different interaction modes of **T1** with RNA, depending on the dye concentration. At low C_{dye}:C_{RNA} ratio, the red species predominates (inset). The pure spectrum in the UV region of this species still resembles that of the initial RNA, which indicates small disruption of its initial structure. The ICD shows positive and negative signals at 440 and 475 nm, respectively, which pointed out to the existence of aggregates. This is of interest since compounds that bind as aggregates have increased binding affinity, increased photostability and selectivity over similar compounds that bind as monomers (Cy5 for example [1]). Upon addition of more ligand, the RNA structure is more disrupted (species depicted in yellow), and concomitantly the mode of interaction changes slightly. These findings correspond to our suggestion for presence of H-aggregates in the solution of **T1**.

Concerning **M1**, the set of CD spectra recorded along the titration of dsDNA with this dye was also well explained with three species (Fig. 1c). The calculated pure spectrum for the intermediate species (shown in

red) also shows an ICD band characterized by positive and negative signals. However, unlike the case of the interaction of **T1** with RNA, several positive and negative signals are observed, which points out to a complex interaction mechanism. Finally, the pure spectra and distribution profiles calculated from the analysis of the spectra recorded along the titration to RNA with **M1** (Fig. 1d) resemble those previously shown for the titration of RNA with **T1** (Fig. 1b). However, small differences were observed at high concentration of dyes, which again pointed out to a more complex mechanism of interaction of **M1** than **T1**.

3.2.3. Fluorescence properties of the dyes

The fluorescence properties of the dyes **M1** and **T1** and their complexes with dsDNA and RNA were studied. The alteration in the fluorescence response of dyes **T1** and **M1** in TE buffer after addition of dsDNA or RNA in increasing concentrations are illustrated in Figs. 3 and 4. It is well known that the homodimers like **TOTO-1** and **BOBO-1** have no fluorescence in water solution due to an intramolecular aggregate induced fluorescence quenching [42]. On the contrary, in our case, some aggregate-induced intrinsic fluorescence of dyes **T1** and **M1** can be detected. Nevertheless, the fluorescence in the presence of dsDNA or RNA increases significantly after aggregate decomposition and the generation of dye-nucleic acid complexes. The deviation, in this case, is the fluorescence maxima at above 520 nm for **T1** and 620 nm for **M1**, which is not typical for commercial analogues like **BO-Pro-1** and **TO**
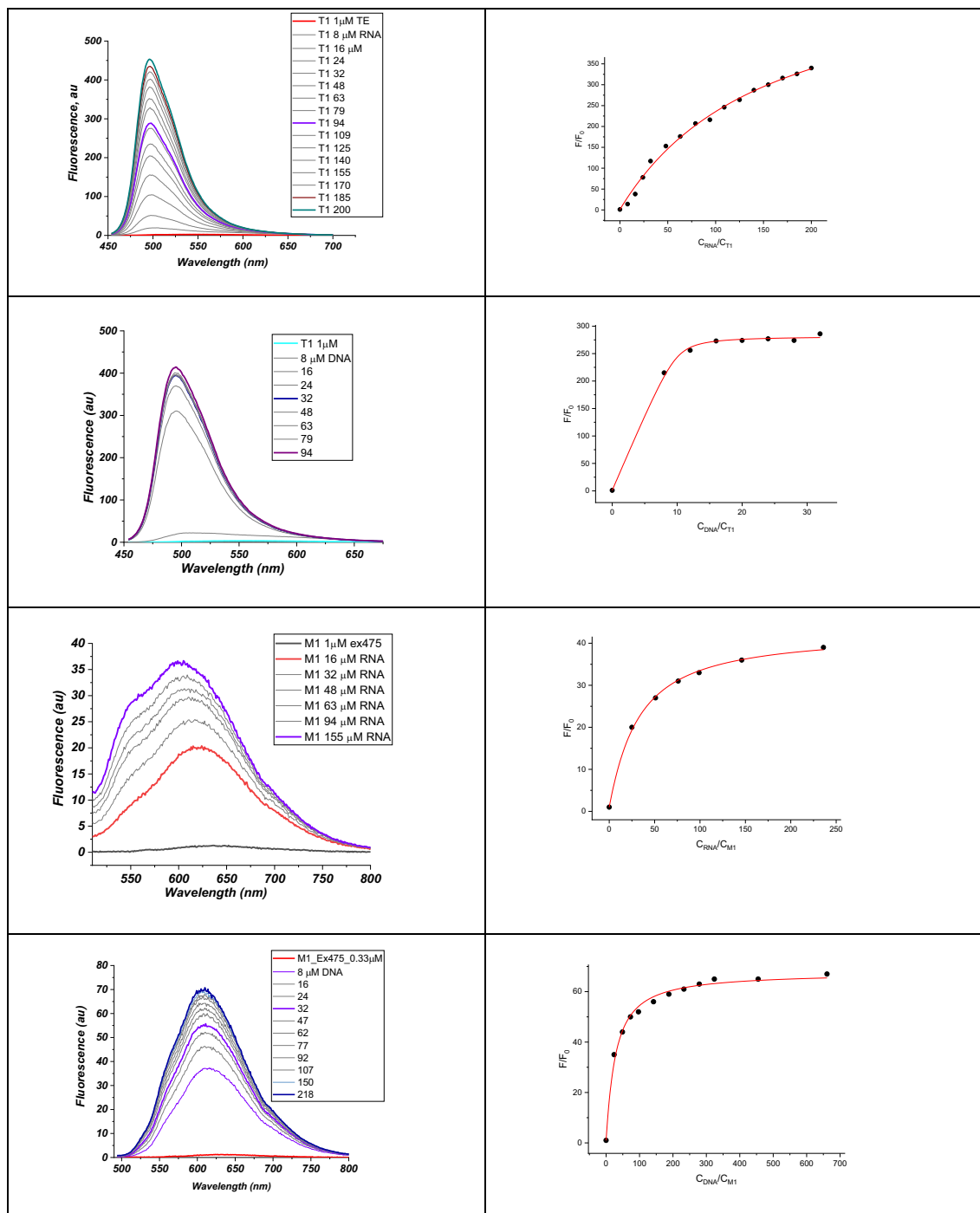
Fig. 3. Fluorescence spectra of **T1** and **M1** dyes in TE buffer neat and in the presence of dsDNA and RNA with increasing concentrations.

monomers [42]. Normally, the fluorescence maxima of the mentioned dyes should be around 480 nm for the **T1** monomer and 530 to 550 nm for the **TO** monomer. The huge and atypical Stokes shift of almost 150 nm caused by the H-aggregates of **T1** and **M1** in solution or on the respective nucleic acid surface is quite favorable for bio-imaging and molecular recognition because such a fluorescence signal is much more informative. This phenomenon allows the use of not only coherent light sources but also LEDs or xenon lamps with a wide excitation spectrum $\Delta\lambda = 20$ nm. Another useful finding is the ratiometric fluorescence response of dye **T1** to RNA compared to that of DNA (Fig. 2a, b) at similar concentrations. Apparently, in TE buffer solution dye **T1** reaches maximum fluorescence much faster with DNA, while with RNA the increase of the fluorescence is smooth and gradual (Fig. 3).

If we compare the fluorescence spectra of dye **T1** with RNA and dsDNA, we see that **M1** fluoresces almost twice as intensely with DNA compared to RNA. It is interesting to note that the fluorescence intensity of dye **T1** in the presence of RNA is several times higher compared to that of **M1** with RNA with commensurable concentrations. Similar is the ratio when comparing **T1** and **M1** fluorescence in the presence of DNA (Fig. 4).

The binding constants for the interaction of the dyes **T1** and **M1** with dsDNA and RNA are determined from the fluorescent titration and given in Table 1. The order of the obtained constants is indicative of the type of binding between the dyes and NA. The values of the binding constants
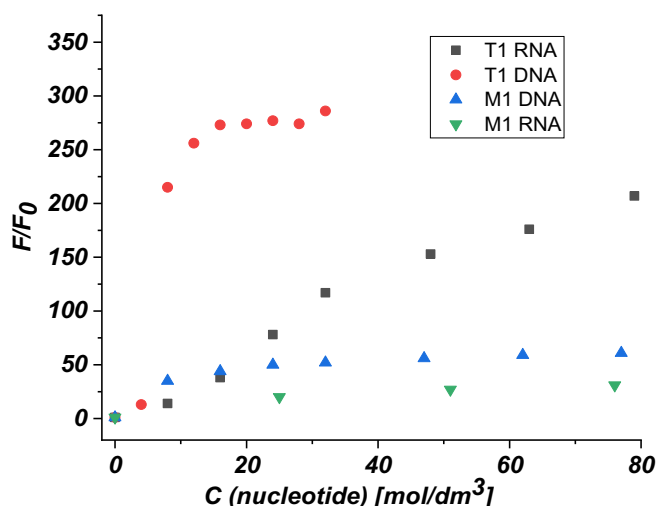
Fig. 4. Changes of the fluorescence emission of **T1** ($c = 1.00 \times 10^{-6}$ mol dm^{-3}) and **M1** ($c = 1.00 \times 10^{-6}$ mol dm^{-3}/$c = 0.33 \times 10^{-6}$ mol dm^{-3}) upon addition of *ds*DNA or RNA at pH 8 (TE buffer).

K_a suggest strong interactions with the nucleic acids and partial inter-calative mode of interaction [4,29]. It is seen from Fig. 3 and Table 1 that the dye **T1** demonstrates higher sensitivity upon excitation.

3.2.4. Salts fluorescence quenching

Most probably the groove binding contributes to the electrostatic hydrogen bonding and hydrophobic interactions [43]. In contrast, the intercalation of small molecules in dsDNA is favored mainly by π-π stacking of the chromophore and the nucleobases [43]. The hydrophobic and the electrostatic interactions ensure additional stabilization for the intercalated dyes. Because of all these complex interactions the precise dye-nucleic acid binding mode is quite difficult to distinguish in

spectroscopic experiments. Therefore, at least several different methods have to be used. According to the method developed by Kumar et al. [43] groove binders can be easily distinguished from the intercalators by titration of the dye-nucleic acid complex with the appropriate salts. According to the authors [43] groove bound small molecules can be released from the dsDNA helix by increasing the ionic strength of the solution. Using the same strategy, we titrated the complexes **T1-NAs** and **M1-NAs** with solutions of potassium iodide and sodium tetra-fluoroborate (Fig. 5) and measured the modulation of the absorption (Fig. 5a) and the fluorescence (Fig. 5b) spectra.

From the absorption spectra of the dye-NA complexes (Fig. 5a), it can be seen that in the corresponding concentration range, the addition of electrolytes leads to a significant decrease in the absorption of the so-lutions. This anisotropy is most probably due to aggregation or even precipitation of the dyes, which is confirmed by the increase in ab-sorption intensity in the whole visible range (Fig. S2). Especially this effect of absorption quenching is stronger with the complexes of the more hydrophobic dye **M1** (Fig. 5a). The analytical techniques based on fluorescence are much more sensitive than the absorption ones. They permit qualitative and quantitative analysis in very low concentrations. Therefore, we consider the fluorescence spectra as more indicative (Fig. 5b). It can be seen from the figure (Fig. 5b) that only in the case of **T1**-RNA complex there is a significant decrease in fluorescence after the addition of potassium iodide or sodium tetrafluoroborate. The **T1**-DNA complex changes its fluorescence only slightly. Similarly, titrating the **M1**-DNA complex with the mentioned electrolytes the fluorescence re-mains relatively stable (Fig. 5b). Similar to above mentioned, upon titration of the **M1**-DNA complex with the commented electrolytes, no significant change in fluorescence was observed (Fig. 5b). In the case of the **M1**-RNA complex, seemingly contradictory results were observed (Fig. 5b). Titration with potassium iodide did not cause significant changes, but titration with sodium tetrafluoroborate provoke significant quenching of the emission. In this case it can be explained by the lower solubility of the hydrophobic tetrafluoroborate compared to the iodide of dye **T1** and its complex. We can conclude that the decrease in the

Table 1

Fluorescence properties - λ_{em}, λ_{ex} in nm, fluorescence intensity of the dyes (I_0) and their complexes with nucleic acids (I) in au, and binding constants (K_a) of **T1** and **M1**.

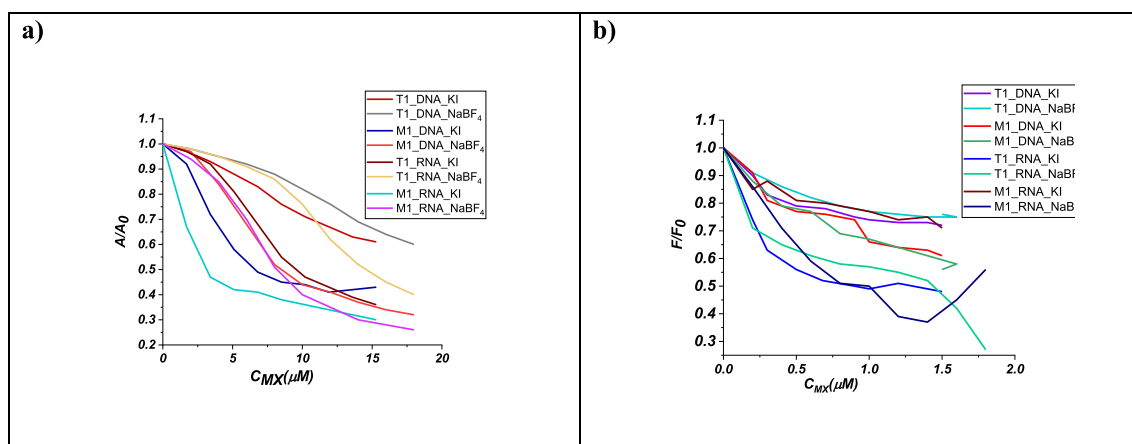| Dye	Neat	Complex with dsDNA						Complex with RNA				
	λ_{em}	λ_{ex}	λ_{em}	I_0	I	I/I_0	K_a	λ_{ex}	λ_{em}	I_0	I	I/I_0	K_a
T1	550	430	495	1.4	415	**286**	$4.6*10^7$	430	496	1.33	453.3	**340**	$0.69*10^5$
M1	627	475	610	1.1	71	**65**	$1.3*10^6$	475	605	0.94	36.7	**39**	$3.8*10^5$

Fig. 5. a) Decrease of the electronic absorption spectra of complexes **T1**-dsDNA, **M1**-dsDNA, **T1**-RNA and **M1**-RNA increasing the concentration of potassium iodide or sodium tetrafluoroborate; **b)** Decrease of the fluorescence intensity of complexes **T1**-dsDNA, **M1**-dsDNA, **T1**-RNA and **M1**-RNA increasing the concentration of potassium iodide or sodium tetrafluoroborate.

fluorescence intensity of **T1**-RNA complex caused by the addition of electrolytes proves the groove binding mode of interaction of the dye with RNA. This is additional evidence for the possibility of both types of binding of the presented new dyes depending on the biomatrix. Stated differently, the formation of the complexes of both dyes (T1, M1) with dsDNA is mainly due to intercalation combined with only partial groove-binding, while the formation of the T1-RNA complex is mainly due to groove-binding.

3.3. Theoretical considerations

DFT and TDDFT calculations were performed in order to rationalize the origin of photophysical properties of the newly synthesized compounds. B3LYP/6-31G(d,p) calculations show that the π-stacked conformers are more stable for **M1** and **T1** homodimers than the optimized extended structures (Fig. 6). It should be mentioned that a number of conformers with a sprawled structure are visible, being very close in energy. The computed Gibbs free energy difference between the stacked and extended **M1** conformers is only 0.4 kcal/mol. Therefore, both conformations exist at ambient conditions thus influencing the photophysical properties of the compounds.

The complexes of the two compounds **M1** and **T1** with DNA were modeled on the basis of 108D PDB structure [47] of DNA oligonucleotide and the bis intercalator TOTO. The model contains four bases CTAG where the ligand intercalates. M062X/6-31G(d,p) optimized **M1**-DNA complexes are shown in Fig. 6. It should be mentioned here that the most popular functionals for geometry optimization B3LYP and PBE are not applicable for DNA optimization because the helical structure of dsDNA is not maintained during the optimization. The two homodimers **M1** and **T1** can act both as mono and bis intercalators considering their extended and stacked conformers respectively. The complex of the **M1** stacked conformer is energetically favored by 1.4 kcal/mol with respect to the **M1** extended conformer, considering the calculated Gibbs free energies.

Photophysical properties of the newly synthesized compounds were estimated using Time-dependent density functional theory (TDDFT). HFS functional combined with 6–31 + G(d,p) basis set was applied. In our previous study, the applicability and accuracy of several DFT functionals for calculating the absorption and fluorescence maxima of monomethine cyanine dyes were assessed [48]. Pure exchange functionals (M06L, HFS, HFB, B97D) were shown to have the best performance during the theoretical evaluation of the absorption and fluorescence characteristics of cyanine dyes. The dyes absorption maxima computed with HFB and HFS functionals appeared to agree very well with the experimental values.

The performed molecular orbitals shape analysis shows the trends of changes in the electron density distribution in the dye molecules and their complexes with DNA. HOMO and LUMO shape representation for the ground and excited states of the stacked conformer of dye **M1** from HFS/6-31G+(d,p) computations in water medium are represented in Fig. 7. The two HOMO orbitals (Fig. 7) are delocalized on the whole molecule, while in LUMO the density is transferred to one part of the homodimer that can be considered as an intramolecular through-space charge transfer (TSCT). This effect cannot be observed in HOMO and LUMO orbitals of the extended conformer. The two monomers in the extended structure are divided by the -CH$_2$PhCH$_2$- group and the charge transfer takes place inside the two monomers from the donor benzo-thiazole part toward the acceptor – quinoline part. For the dye-DNA complexes the lowest energy transition with nonzero oscillator strength involves both DNA and ligand orbitals (Fig. 7).

The interaction energies of ligands as mono intercalators with long dsDNA and dsRNA models of 1XRW were obtained by docking studies. The results show that **M1** intercalates equally well within both nucleic acids. We did not find an adequate model of **T1** in dsRNA as during the induced fit the nucleic acid structure was strongly disturbed. In both dsDNA and dsRNA models, **T1** interacts with the double-strand nucleic acid as bis intercalator. **M1** spontaneously forms bis intercalation with the lowest energy only in the case of dsDNA. Low energy complexes are formed in many cases when shorter nucleic acids were used, mainly as a consequence of the interaction of the ligand with the end of the nucleic acid or due to easier displacement of nucleobases at the ends of nucleic acids. Ligands are tested for their ability for bis intercalation in models with gaps, which are 1,2,3, or 4 nucleobases apart. The difference between interaction energies of ligands as bis intercalators with long dsDNA and dsRNA models of 1Z3F reveals that **M1** and **T1** preferably bind to dsDNA that is in accordance with the experimental binding constants (Table 2). This deviation between dsDNA and dsRNA is more pronounced for **T1** that is also in agreement with spectroscopic measurements (Table 2).

After the induced fit docking and the following minimization step, the nearest local minima can be reached. A series of molecular dynamics
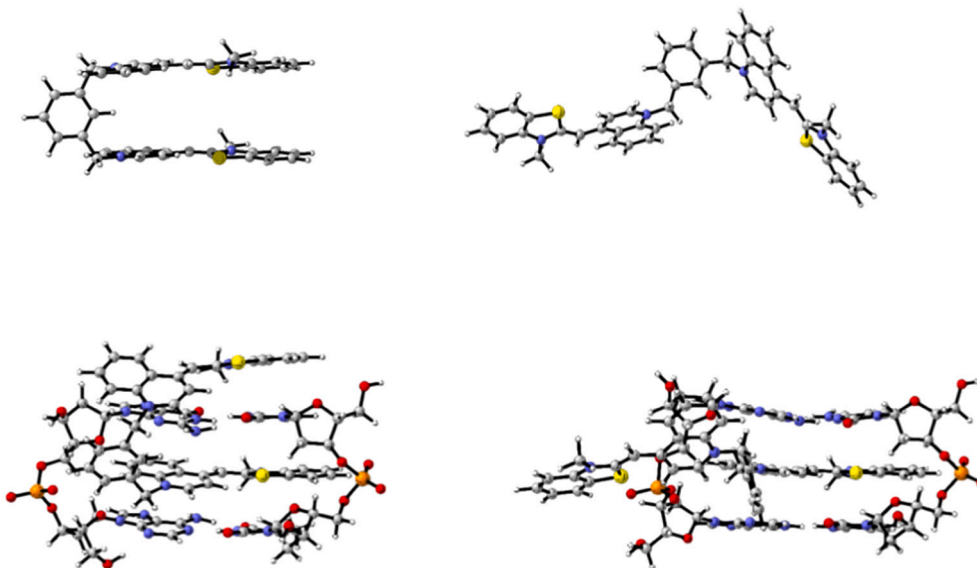

Fig. 6. PCM B3LYP/6–31 + G(d,p) optimized conformers in water medium for the dye **M1**: π-stacked (A) and extended (B) structures, and respective DNA complexes (C, D) from M062X/6-31G(d,p) calculations. Colour scheme: grey – carbon atoms; blue – nitrogen atoms; yellow – sulfur atoms. (For interpretation of the references to colour in this figure legend, the reader is referred to the web version of this article.)
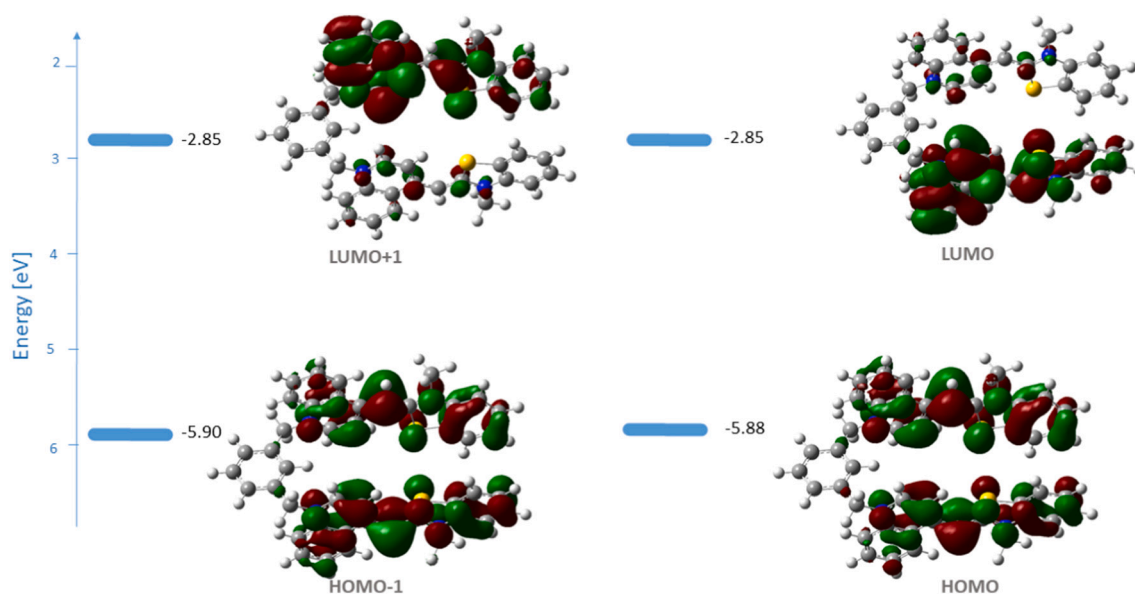
Fig. 7. HOMO and LUMO shape representation for the ground and excited states of the stacked conformer of dye **M1** from HFS/6-31G+(d,p) computations in water medium. The exact energies of LUMO and LUMO+1 orbitals are −2.852319912 eV and − 2.849598752 eV respectively.

Table 2

HFS/6–31 + G(d,p) calculated (in water medium) and experimental (in TE buffer) absorption maxima for **M1** and **T1** dyes (ligands) and their complexes with DNA. The oscillator strength is given in parentheses.

Dye	Ligand		DNA-Ligand complex	
	λ_{calc}	λ_{exp}	λ_{calc}	λ_{exp}
M1	497 (1.48)	505	512 (0.70)	508
M1stacked	479 (1.55)	475	508 (0.71)	479
T1	441 (2.08)	456	474 (0.78)	460
T1stacked	427 (1.35)	428	443 (0.57)	430

simulations with our best hits obtained after minimization was performed in order to check for deeply located minima on the potential energy surface of the complexes. AMBER12EHT force field and NAMD software package were used. The protocol uses explicit water molecules in periodic boundary conditions at 300 K, 101 kPa. The last frame of 150 ns MD trajectories was further cooled to 100 K and after that water molecules were removed and the complex was minimized using AMBER12EHT with the generalized Born solvation model. The interaction energy of a ligand with nucleic acid was calculated by applying GBVI/WSA scoring function on the minimized complexes. The interaction energies of **M1** and **T1** ligands with dsDNA and dsRNA from MD simulations are given in Table 3.

It can be seen from Table 3 that **T1** prefers to be a bis intercalator with gap 2 (Fig. 8A), while **M1** favours being bis intercalator with gap 1 (Fig. 8B), both in dsDNA. **T1** promotes forming bis intercalation complexes with both dsDNA and dsRNA, but some variation exists – the interaction with dsDNA shows that the preferred gap is 2, while dsRNA goes for gap1. **T1** prefers to interact with dsDNA compared to dsRNA with 1.0 kcal/mol. Invariably, the minor groove interaction (Fig. 8C) is favored over the major groove interaction. It should be mentioned that complexes with the minor groove of dsRNA are less favorable for the studied ligands due to the disadvantageous interaction with 2′OH ribose groups, which makes dsRNA minor groove more hydrophilic in comparison to the dsDNA minor groove. When the ligands interact as single (mono) intercalators, they prefer to enter between nucleobases with one of their ends and to place the rest of the molecule in the minor groove (Fig. 8D), instead of intercalating their central part and interacting with their ends with the minor and respectively with the major groove (Fig. 8E).

Table 3

Interaction energies of **M1** and **T1** ligands with dsDNA and dsRNA.

Dye	dsDNA		dsRNA	
	ΔE [kcal/mol]	Type of interaction	ΔE [kcal/mol]	Type of interaction
M1	−13.03	Mono intercalation (center)	−15.54	Mono intercalation (center)
	−14.09	Mono intercalation (end)		
	−17.40	Bis intercalation gap 1	**−15.95**	Bis intercalation gap 1
			−14.48	Bis intercalation gap 2
	−16.52	Groove binding	−10.41	Groove binding
T1	−10.23	Mono intercalation (center)	−12.18	Mono intercalation (end)
			−10.62	Mono intercalation (end)
	−13.60	Bis intercalation gap 1	**−14.24**	Bis intercalation gap 1
	−15.27	Bis intercalation gap 2	−12.97	Bis intercalation gap 2
	−15.15	Groove binding	−10.07	Groove binding (center)

3.4. Fluorescence imaging of living cells

After adding dye **M1** SCAPs cells in final concentrations of 2 and 20 μM we observed penetration through the cellular membrane. Although the 2 μM concentration seemed not to be sufficient for nuclear membrane penetration, the 20 μM dye stained the cell nuclei (Fig. 9).

After 5 days in the presence of **M1** (20μM), the cells were still alive and dividing, showing that the dye remained in the mother cells - in the endoplasmic reticulum rather than in the daughter cells. MTT test (Fig. 9 C) did not show significant change in cell division rate ($p > 0.05$). The concentration of the dye has decreased significantly and is hardly noticeable in the new cells. According to the data analysis of In Cell Analyzer 6000, the maximum fluorescence intensity of the dye **M1** is detected mainly at excitation of 488 nm and emission at 605 ± 52 nm, as well as at 706 ± 72 nm (Fig. 10A). The highest signal intensity is observed at 48 h after incubation with the dye. The **M1** dye showed higher intensity than the control with Hoechst 33342 in all three
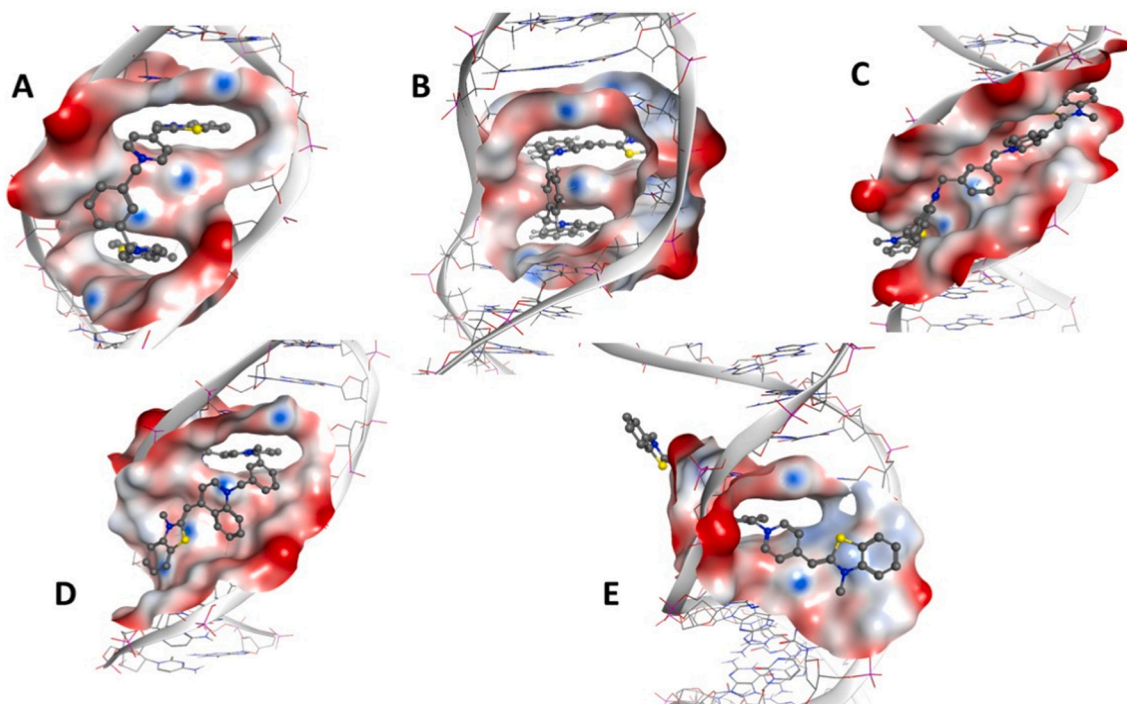
Fig. 8. Bis intercalation (A, B), groove binding (C), and mono intercalation (D, E) of **M1** to dsDNA from MD simulations.
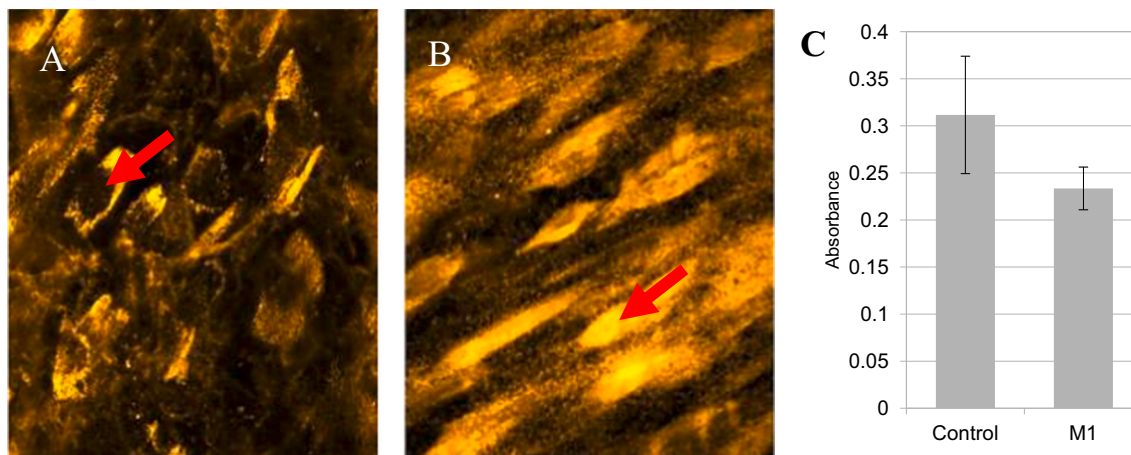

Fig. 9. Fluorescence image of SCAPs treated with 2×10^{-6} M **M1** dye. Magnification 60×. After 24 h (A) and 72 h (B). Cell absorbance after MTT test, no significant difference was found with paired *t*-test ($p > 0.05$) (C). Red arrows indicate nuclei. (For interpretation of the references to colour in this figure legend, the reader is referred to the web version of this article.)
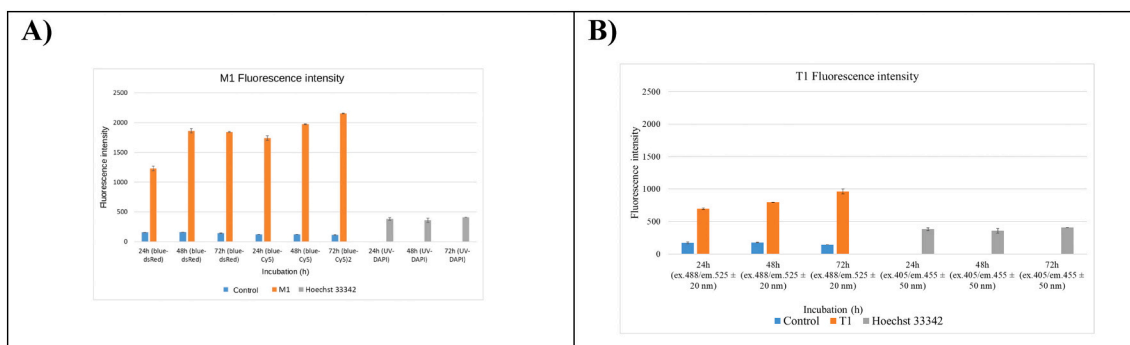

Fig. 10. A) Fluorescence intensity of **M1** in living cells measured by In Cell Analyzer 6000; **B)** Fluorescence intensity of **T1** in living cells measured by In Cell Analyzer 6000.

detection tests (after 24 h, 48 h, and 72 h of incubation). To shed light on the selectivity of dyes **T1** and **M1** to definite cell compartments we measured their fluorescence in presence of BSA in bulk (Fig. S8). In the presence of BSA, the fluorescence of the **M1** dye significantly increased (Fig. S8), while with dye **T1** there was no indication for interaction with the protein. Based on this experiment we can speculate that **M1** probably binds proteins in the cytoskeleton.

The fluorescence intensity of **T1** in living cells was significantly higher compared to the auto-fluorescence of the control cells. It showed also higher fluorescence intensity than the widely used reference dye Hoechst 33342 (Fig. 10B). Examination of **T1** fluorescence in living cells shows that the dye is best detected upon excitation at 488 nm. The emission is most prominent in the range 525 ± 20 nm. As the incubation time increases, the fluorescence intensity also increases, with the highest values on the 3rd day. This makes **T1** suitable for use in fluorescence detection of living cell cultures.

Fluorescence confocal microscopy images showed that hydrophobic **T1** penetrates the intact living SCAP cell membrane in final concentrations of 1 μM and binds to cytoplasmic components. The dye was staining granular structures positioned around the cell nucleus, and this observation is possibly due to binding to RNA-rich cell structures like ribosomes in the free state or in the endoplasmic reticulum (ER), which differs from the pattern observed in the fluorescence images of cells treated with **M1** (Fig. 11A, B). The binding of **T1** to RNA was supported by the spectral data from nucleic acid titrations indicating the affinity of the dye for RNA. In contrast to **M1**, at **T1** there are no visible dynamics in the fluorescence signal of the dye. Cells continued to divide throughout the duration of the experiment (72 h) and visually **T1** did not lead to necrosis and disattachment of SCAPs. The performed MTT analysis (Fig. 11C) showed decreased cell division rate (p > 0.05).

3.5. Fluorescence imaging of formalin-fixed cells

In SCAP fixed with 4 % (*w/w*) formalin, the **M1** dye has a strong fluorescence excitation at 488 nm with a wide emission spectrum from 525 to 778 nm. The fluorescence intensity of **M1** exceeds those of DAPI used as a control dye (Fig. 12A). When fluorescence was observed in the range 605 ± 52 nm, the dye was found only in the cytoplasm. **M1** penetrates the cell membranes of fixed cells and clearly delineates the nuclei, as seen at the emission of 525 ± 20 nm (Fig. 12B).

T1 dye in fixed cells is excited at 405 nm and 488 nm and emits a signal in the range of 525 ± 20 nm and 605 ± 52 nm (Fig. 12C). The emission in the green region upon irradiation at 488 nm is strong, clearly distinguishing that **T1** binds to cytoplasmic components. In fixed cells, when the integrity of the nuclear membrane is disrupted, we found that **T1** enters the nucleus directly, but apparently does not interact with

DNA and binds in the RNA-rich nucleoli. This result was also confirmed by the spectral data after titration with RNA, in which binding of the **T1** dye to RNA was observed. According to these data, **T1** also binds to dsDNA, but in vitro, the dye does not show similar selectivity (Fig. 12D). Due to the absence of metabolic activity in the fixed cells, no binding dynamics were observed, and the dye directly stained cytoplasmic contents and nuclei. Taken together, studies of **T1** in live and fixed cells support the suggestion that **T1** has a marked affinity for RNA-rich cellular structures, i.e. nucleoli or ribosomes.

In order to clarify the possible influence of formalin on the RNA structures, we measured the fluorescence of the **T1-RNA** complex in pure form or in the presence of formalin in bulk. It can be seen from Fig. S9 that in the presence of 20 % formalin in the solution, the fluorescence of the dye drops insignificantly. This can be taken as evidence that formalin does not affect the state of the **T1-RNA** complex in the given conditions.

Long term cultivation of SCAP with the **M1** and **T1** dyes did not cause direct necrosis and cellular disattachment. Although **T1** affected the cell rate, with both dyes the cells continued to divide actively and showed high photochemical stability in living SCAPs, as well allowed us to determine their potential for obtaining images of biological objects in vitro. The results of fluorescence signal measurement do not significantly depend on intracellular optical inhomogeneity. Significant differences between **T1** and **M1** cellular structures binding was observed. Although both dyes being homodimers, they have shown different protein binding activity (Fig. S8). For **M1** it was found to predominantly dye cellular organelles resembling the cytoskeleton and ER. Further into entering the cell membrane and the dye transfusing in the cytosol the specific bond to the cytoskeleton disappears and the dye reappears at the ER, where it is finally bound. These observations propose active cytoskeleton transportation and storage of **M1** dye in the ER. **T1** dye readily passed through the cell membrane and stained cytoplasmic structures but unlike **M1** dye it, passed the nuclear membrane of living cells staining nuclear structures after 72 h in non-toxic concentrations.

Both dyes performed differently yet when formalin fixed cells were stained. **M1** dye was found to specifically concentrate and stain cellular nucleus without significant cytoplasmic binding thus giving sufficient contrast for cyto-fluorescent staining. **T1** on other hand still bound to cytoplasmic protein structures but quickly entered the nucleus and concentrated in structures strongly resembling nucleoli. Somewhat surprising for us was the lack of staining in the entirety of the cellular nucleus. Spectral and living cellular data showed affinity of the dye for DNA which seems to extinguish after formalin fixation. This result is encouraging for further investigations specifically for RNA and DNA specificity of **T1** after formalin fixation. Colocalization tests for nucleoli and ribosomes of fixed cells stained with **T1, which** can for certain
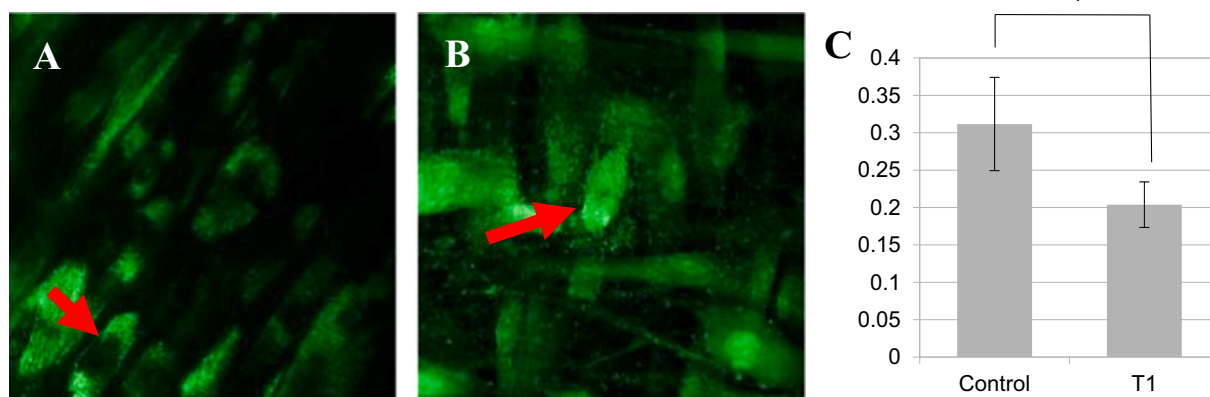

Fig. 11. Fluorescence image of SCAPs treated with 10^{-6} M **T1** dye. Magnification 60×. After 24 h (**A**) and 72 h (**B**); **C**) MTT analysis of SCAP stained with **T1** (2×10^{-6} M). Statistical significance was found with paired t-test * (*p* < 0.05). Red arrows indicate nuclei. (For interpretation of the references to colour in this figure legend, the reader is referred to the web version of this article.)
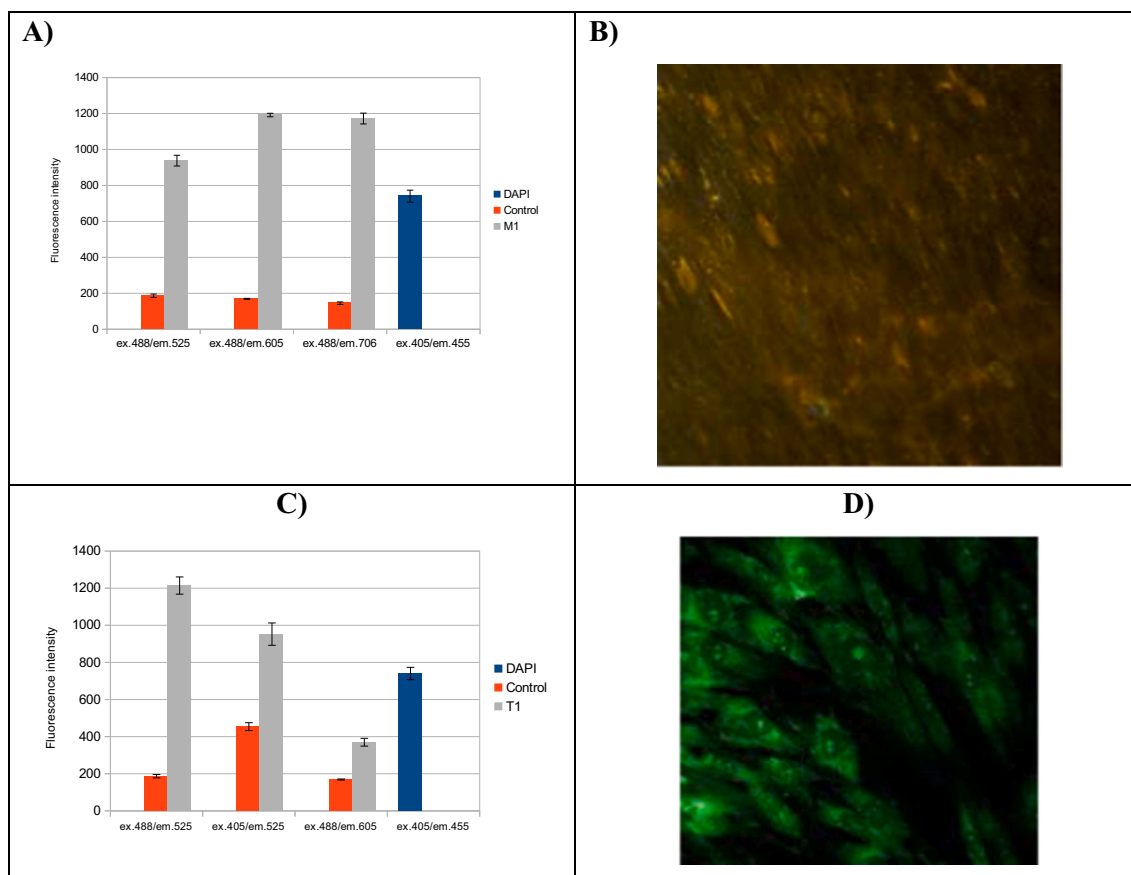
Fig. 12. A) Fluorescence intensity of **M1** in formalin-fixed cells measured by In Cell Analyzer 6000; **B**) Fixed SCAP, stained with 2×10^{-6} M **M1** dye. Magnification $60\times$; **C**) Graph representing maximum fluorescence intensity of formalin-fixed SCAP P7 cells treated with **T1** dye (10^{-6} M) by In Cell Analyzer 6000 confocal fluorescence microscope after 24 h. Comparison of **T1** intensity with the reference dye DAPI (10^{-8} M). Untreated cells were used as controls; **D**) Fixed SCAP, stained with 10^{-6} M **T1** dye. Magnification $60\times$.

prove our assumption that **T1** dye specifically stains RNA are planned.

4. Conclusion

In order to improve the existing methods of fluorescent detection, the development of new fluorescent dyes is an always persisting goal. We developed two new homodimeric asymmetric monomethine cyanines with relatively small structural differences but expressing versatile staining properties with superior fluorescent intensity. Both newly synthesized dyes were proven not to be toxic for living cells in sufficient concentrations for fluorescent staining. **M1** was found to have affinity to cytozolic structures and not to penetrate the nuclear membrane of the living cells. **T1** on the other hand penetrated it in non-toxic higher concentrations and stained the whole nucleus. Formalin fixation changed dramatically the cellular penetration and affinity of both dyes, yet again differently. **M1** stained predominantly cellular nucleus, whereas **T1** markedly stained only small area of the nuclei resembling structures like nucleoli. Thus, we speculate **T1** has RNA binding affinity in formalin fixed cells. We defined the different staining properties of these dyes according to the conditions that open multiple possibilities for future application in numerous methods requiring the use of fluorescent probes.

CRediT authorship contribution statement

Project administration, methodology for work with SCAP, data curation, writing – review and editing – N.I., methodology – V.M.; validation – T.S.; formal analysis, investigation – Z.M.; writing – original draft preparation, methodology – M.M. and M.M.; HPLC-MS analysis – V.V.L., V.S.L.; synthesis of the heterocyclic intermediates, purification of the intermediates, methodology – M.K.; writing – original draft preparation, writing – review and editing – B.C.; theoretical considerations, writing and editing; validation, writing – D.V., S.I. M.R. N.T.; Circular dichroism, MCR-ALS method, writing, validation – R.G.; validation of the analysis – S.B., K.L.; supervision – I.C.; project administration, design of the structures, synthesis and purification of the dyes, characterization of the structures, photo-physical properties, supervision, funding acquisition, validation, writing – A.V.

Declaration of competing interest

The authors declare that they have no known competing financial interests or personal relationships that could have appeared to influence the work reported in this paper.

Data availability statement

Not applicable.

Appendix A. Supplementary data

Supplementary data to this article can be found online at https://doi.org/10.1016/j.ijbiomac.2023.126094.

References

[1] A guide to fluorescent probes and labeling technologies, in: Molecular Probes, 11th Ed, Thermo-Fisher, Eugene, OR, 2010.

[2] M. Kubista, J. Karlsson, M. Bengtsson, N. Zoric, G. Westman, Chapter 10. DNA-binding fluorophores, in: S.O. Rogers (Ed.), Molecular Analyses, Medical Genomics and Proteomics Series, Charles R. Crumly, CRC Press/Taylor & Francis Group, Boca Raton, London, New York, 2022, https://doi.org/10.1201/9781003247432-10, pp. 97-7.

[3] I. Fabijani'c, A. Kurutos, A. Pai'c, V. Tadi'c, F.S. Kamounah, L. Horvat, A. Brozovic, I. Crnolatac, M. Radi'c Stojkovi'c, Selenium-substituted monomethine cyanine dyes as selective G-quadruplex spectroscopic probes with Theranostic potential, Biomolecules 128 (13) (2023) 1, https://doi.org/10.3390/biom13010128.

[4] I. Zonjic, M.S. Radic, I. Crnolatac, A.P. Tomasic, S. Psenicnik, A. Vasilev, M. Kandinska, M. Mondeshki, S. Baluschev, K. Landfester, L. Glavaš-Obrovac, M. Jukić, J. Kralj, A. Brozovic, L. Horvat, Lidija-Marija Tumira, Styryl dyes with N-Methylpiperazine and N-Phenylpiperazine functionality: AT-DNA and G-quadruplex binding ligands and theranostic agents, Bioorg. Chem. 127 (2022), 105999, https://doi.org/10.1016/j.bioorg.2022.105999.

[5] T. Deligeorgiev, A. Vasilev, Cyanine dyes as fluorescent non-covalent labels for nucleic acid research, in: K. Sung-Hoon (Ed.), Functional Dyes, Elsevier, 2006, pp. 137–183.

[6] M. He, Y. Sato, S. Nishizawa, Classical thiazole orange and its regioisomer as fluorogenic probes for nucleolar RNA imaging in living cells, Analyst 148 (2023) 636–642, https://doi.org/10.1039/D2AN01804G.

[7] M.M. Mhlanga, D.Y. Vargas, C.W. Fung, F.R. Kramer, S. Tyagi, tRNA-linked molecular beacons for imaging mRNAs in the cytoplasm of living cells, Nucleic Acids Res. 33 (2005) 1902, https://doi.org/10.1093/nar/gki302.

[8] B.J. Zhou, W.M. Liu, H.Y. Zhang, J.S. Wu, S. Liu, H.T. Xu, P.F. Wang, Imaging of nucleolar RNA in living cells using a highly photostable deep-red fluorescent probe, Biosens. Bioelectron. 68 (2015) 189, https://doi.org/10.1016/j.bios.2014.12.055.

[9] Y. Liu, W.J. Zhang, Y.M. Sun, G.F. Song, F. Miao, F.Q. Guo, M.G. Tian, X.Q. Yu, J. Z. Sun, Two-photon fluorescence imaging of RNA in nucleoli and cytoplasm in living cells based on low molecular weight probes, Dyes Pigments 103 (2014) 191, https://doi.org/10.1016/j.dyepig.2013.12.005.

[10] G.F. Song, Y.M. Sun, Y. Liu, X.K. Wang, M.L. Chen, F. Miao, W.J. Zhang, X.Q. Yu, J. L. Jin, Low molecular weight fluorescent probes with good photostability for imaging RNA-rich nucleolus and RNA in cytoplasm in living cells, Biomaterials 35 (2014) 2103, https://doi.org/10.1016/j.biomaterials.2013.11.052.

[11] Q. Li, Y.Y. Kim, J.S. Namm, A. Kulkarni, G.R. Rosania, Y.-H. Ahn, Y.-T. Chang, Calcium-dependent ligand binding and G-protein signaling of family B GPCR parathyroid hormone 1 receptor purified in nanodiscs, Chem. Biol. 13 (2006) 615, https://doi.org/10.1021/cb300466n.

[12] A. Renaud de la Faverie, A. Guedin, L.A. Bedrat, J.L. Mergny Yatsunyk, Thioflavin T as a fluorescence light-up probe for G4 formation, Nucleic Acids Res. 42 (8) (2014) 65, https://doi.org/10.1093/nar/gku111.

[13] S. Gohla, et al., Encapsulation of retinoids in solid lipid nanoparticles (SLN), J. Microencapsul. 18 (2001) 149–158, https://doi.org/10.1080/02652040010000361.

[14] Y.J. Lu, Q. Deng, D.P. Hu, Z.Y. Wang, B.H. Huang, Z.Y. Du, Y.X. Fang, W.L. Wong, K. Zhang, C.F. Chowm, A molecular fluorescent dye for specific staining and imaging of RNA in live cells: a novel ligand integration from classical thiazole orange and styryl compounds, Chem. Commun. 51 (2015) 15241–15244, https://doi.org/10.1039/C5CC05551B.

[15] A.J. Hiscox, RNA viruses: hijacking the dynamic nucleolus, Nat. Rev. Microbiol. 5 (2007) 119–127, https://doi.org/10.1038/nrmicro1597.

[16] M. Hetman, Role of the nucleolus in human diseases. Preface, Biochim. Biophys. Acta 1842 (6) (2014) 757, https://doi.org/10.1016/j.bbadis.2014.03.004.

[17] M. Bahadori, M.H. Azizi, S. Dabiri, N. Bahadori, Effects of human nucleolus upon guest viral-life, focusing in COVID-19 infection, Iran. J. Pathol. 17 (1) (2022) 1–7, https://doi.org/10.30699/IJP.2021.540305.2744.

[18] J.E. Quin, J.R. Devlin, D. Cameron, K.M. Hannan, R.B. Pearson, R.D. Hannan, Targeting the nucleolus for cancer intervention, Biochim. Biophys. Acta Mol. basis Dis. 1842 (6) (2014) 802–816, https://doi.org/10.1016/j.bbadis.2013.12.009.

[19] S.J. Woods, K.M. Hannan, R.B. Pearson, R.D. Hannan, The nucleolus as a fundamental regulator of the p53 response and a new target for cancer therapy, Biochim. Biophys. Acta, Gene Regul. Mech. 1849 (7) (2015) 821–829, https://doi.org/10.1016/j.bbagrm.2014.10.007.

[20] W. Zakrzewski, M. Dobrzyński, M. Szymonowicz, Z. Rybak, Stem cells: past, present, and future, Stem Cell Res Ther 10 (1) (2019) 1–22.

[21] M. Saleh, A. Movassaghpourakbari, P. Akbarzadehlaleh, Z. Molaeipour, The impact of mesenchymal stem cells on differentiation of hematopoietic stem cells, Adv. Pharm. Bull. 5 (3) (2015) 299, https://doi.org/10.15171/2Fapb.2015.042.

[22] L. Gan, Y. Liu, D. Cui, Y. Pan, L. Zheng, M. Wan, Dental tissue-derived human mesenchymal stem cells and their po-tential in therapeutic application, Stem Cells Int. Sep 1 (2020), 8864572, https://doi.org/10.1155/2020/8864572.

[23] M.L. Couble, J.C. Farges, F. Bleicher, B. Perrat-Mabillon, M. Boudeulle, H. Magloire, Odontoblast differentiation of human dental pulp cells in explant

[24] cultures, Calcif. Tissue Int. 66 (2) (2000) 129–138, https://doi.org/10.1007/pl00005833.

[24] N. Ishkitiev, K. Yaegaki, A. Kozhuharova, T. Tanaka, M. Okada, V. Mitev, M. Fukada, T. Imai, Pancreatic differentia-tion of human dental pulp CD117+ stem cells, Regen. Med. 8 (5) (2013) 597–612, https://doi.org/10.2217/rme.13.42.

[25] N. Ishkitiev, K. Yaegaki, T. Imai, T. Tanaka, N. Fushimi, V. Mitev, M. Okada, S. O. Tominaga, H. Ishikawa, Novel management of acute or secondary biliary liver conditions using hepatically differentiated human dental pulp cells, Tissue Eng. A 21 (3–4) (2015) 586–593, https://doi.org/10.1089/ten.tea.2014.0162.

[26] I. Crnolatac, L.M. Tumir, N.Y. Lesev, A.A. Vasilev, T.G. Deligeorgiev, K. Mišković, L. Glavaš-Obrovac, O. Vugrek, I. Piantanida, Probing the structural properties of DNA/RNA grooves with sterically restricted phosphonium dyes: screening of dye cytotoxicity and uptake, ChemMedChem 8 (7) (2013) 1093–1103, https://doi.org/10.1002/cmdc.201300085.

[27] L.M. Tumir, I. Crnolatac, T. Deligeorgiev, A. Vasilev, S. Kaloyanova, M. Grabar Branilović, I. Piantanida, Kinetic differentiation between homo- and alternating AT DNA by sterically restricted Phosphonium dyes, EChemistry–A uropean Journal 18 (13) (2012) 3859–3864, https://doi.org/10.1002/chem.201102968.

[28] A.S. Tatikolov, Photochemistry reviews, J Photochem Photobiol C: Photochem Rev 13 (2012) 55–90, https://doi.org/10.1016/j.jphotochemrev.2011.11.001.

[29] I. Mikulin, I. Ljubi'c, I. Piantanida, Aleksey Vasilev, Mihail Mondeshki, Meglena Kandinska, Lidija Uzelac, Irena Martin-Kleiner, Marijeta Kralj, Lidija-Marija Tumir, Biomolecules 11 (2021) 1075, https://doi.org/10.3390/biom11081075.

[30] A. Kurutos, T. Ilic-Tomic, F.S. Kamounah, A.A. Vasilev, J. Nikodinovic-Runic, J. Photochem. Photobiol. A Chem. 397 (2020) 112598, https://doi.org/10.1016/j.jphotochem.2020.112598.

[31] M.I. Kandinska, D.V. Cheshmedzhieva, A. Kostadinov, K. Rusinov, M. Rangelov, N. Todorova, A.A. Vasilev, Tricationic asymmetric monomeric monomethine cyanine dyes with chlorine and trifluoromethyl functionality–FLUOROGENIC nucleic acids probes, J. Mol. Liq. 342 (2021), 117501, https://doi.org/10.1016/j.molliq.2021.117501.

[32] A. Mishra, R.K. Behera, P.K. Behera, B.K. Mishra, G.B. Behera, Cyanines during the 1990s, Chem. Rev. 100 (6) (2000) 1973–2012, https://doi.org/10.1021/cr990402t.

[33] a) N.A. Zhao, M. Wang, X. Niu, W. Sun, K. Jiao, J. Chil. Chem. Soc. 53 (3) (2008);
b) M. Frances, Hamer in "the Cyanine Dyes and Related Compounds" from "the Chemistry of Heterocyclic Compounds", in: A Series of Monographs, Arnold Weissberger, Interscience publishers, John Wiley and Sons, New York, London, 1964.

[34] H. Edelsbrunner, M. Facello, R. Fu, J. Liang, Measuring proteins and voids in proteins, in: Proceedings of the 28th Hawaii International Conference on Systems Science, 1995, pp. 256–264, https://doi.org/10.1109/HICSS.1995.375331.

[35] Molecular Operating Environment (MOE), 01; Chemical Computing Group ULC, 1010 Sherbooke St. West, Suite #910, Montreal, QC, Canada, H3A 2R7, 2021. https://www.chemcomp.com/index.htm, 2019.

[36] a) C.H.G. Williams, Trans. Roy. Soc. Edinburg 21 (1856) 377;
b) C.H.G. Williams, Chem. News 1 (1859) 15;
c) C.H.G. Williams, Chem. News 2 (1860) 219;
d S. Hoogewerff, W.A. van Drop, Rec. Trav. Chim. 2 (a) 28 (b) (1883) 41;
e S. Hoogewerff, W.A. van Drop, Rec. Trav. Chim. (1884) (a) 2, 317 (1883); (b) 3, 335;
f) W. Spalteholz, Ber. 16 (1883) 1847.

[37] L.G.S. Brooker, G. Kyers, W. Willidms, J. Am. Chem. Sos. 64 (1942) 199.

[38] US Patent 5321130, 1994. US Patent 5436134 (1995).; US Patent 5658751 (1997).

[39] T.G. Deligeorgiev, D. Zaneva, H. Katerinopulos, V. Kolev, Dyes Pigments 41 (1999) 49–54, https://doi.org/10.1016/S0143-7208(98)00061-8.

[40] T.G. Deligeorgiev, D. Zaneva, S.M. Kim, Dyes and Pigments 17, 1998, p. 205. S0143-7 208(98)00046-1.

[41] A. Vasilev, T. Deligeorgiev, S. Kaloyanova, S. Stoyanov, V. Maximova, J. J. Vaquero, J. Alvarez-Builla, Synthesis of novel tetracationic asymmetric monomeric monomethine cyanine dyes – highly fluorescent dsDNA probes, Color. Technol. 127 (1) (2011) 69–74, https://doi.org/10.1111/j.1478-4408.2010.00280.x.

[42] W. Sabnis, Handbook of Biological Dyes and Stains, John Wiley & Sons, Inc, Hoboken, New Jersey, USA, Canada, 2010, p. 51.

[43] C.V. Kumar, R.S. Turner, E.H. Asuncion, Groove binding of a styrylcyanine dye to the DNA double helix: the salt effect, J. Photochem. Photobiol. A Chem. 74 (1993) 231–238, 1010-6030/93/$6.00.

[44] E.W. White, F. Tanious, M.A. Ismail, A.P. Reszka, S. Neidle, D.W. Boykin, W. Wilson, Structure-specific recognition of quadruplex DNA by organic cations: influence of shape, substituents and charge, Biophys. Chem. 126 (2007) 140–153, https://doi.org/10.1016/2Fj.bpc.2006.06.006.

[45] M. Wang, G.L. Silva, B.A. Armitage, DNA-templated formation of ahelical cyanine dye J-aggregate, J. Am. Chem. Soc. 122 (2000) 9977–9986, https://doi.org/10.1021/ja002184n.

[46] J. Jaumot, R. Gargallo, A. de Juan, R. Tauler, A graphical user-friendly interface for MCR-ALS: a new tool for multivariate curve resolution in MATLABChemometrics and Intel, Lab. Systems 76 (1) (2005) 1–110, https://doi.org/10.1016/j.chemolab.2004.12.007.

[47] H.P. Spielmann, D.E. Wemmer, J.P. Jacobsen, Solution structure of a DNA complex with the fluorescent bis-intercalator TOTO determined by NMR spectroscopy, Biochemistry. 34 (27) (1995) 8542–8553, https://doi.org/10.1021/bi00027a004.

[48] S. Ilieva, M. Kandinska, A.A. Vasilev, D. Cheshmedzhieva, Theoretical modeling of absorption and fluorescent characteristics of cyanine dyes, Photochem. 2 (1) (2022) 202–216, https://doi.org/10.3390/photochem2010015.